REVIEW ARTICLE

Check for updates

A review on the recent advances in the design and structure–activity relationship of TiO₂-based photocatalysts for solar hydrogen production

Sunesh S. Mani, [a] Sivaraj Rajendran, [a] Thomas Mathew *[a] and Chinnakonda S. Gopinath *[bc]

The major issues that determine the efficiency of photocatalyst composite materials for solar hydrogen production, with or without a sacrificial agent, are efficient visible light harvesting properties, efficient separation of charge carriers and their utilization of redox sites, and stability. Thus, significant efforts have been devoted in the past few decades to modify the above characteristics by integrating constituent components of composites using different approaches. In the present review, we aim to summarize the recent advances, predominantly, in the area of TiO₂-based photocatalyst composites for solar hydrogen production. Firstly, we present the recent progress in material integration aspects by discussing the integration of TiO₂ with different categories of materials, including noble/3d metals, metal oxides/sulphides/selenides, other low bandgap semiconductors, C-based materials, and dye sensitizers. Furthermore, we discuss how material integration helps in tailoring the electronic and optical properties for activity tuning in solar H₂ production. Subsequently, critical changes in the physico-chemical and electronic properties of composites with respect to their preparation methods, morphology, crystallographic facets, particle size, dopant, calcination temperature, and structure–activity relationship to solar hydrogen production are addressed in detail. Moreover, we discuss the importance of fabricating a photocatalyst in a thin film form and performing solar hydrogen production in different reactor set-ups for enhancing its photocatalytic performance, while addressing device scalability. Despite the significant advancements made in this field, solar-to-hydrogen conversion efficiency still needs to be improved to realise the practical application of solar hydrogen production. In this case, the direct conversion of water to hydrogen *via* overall water splitting and renewable H₂ production from wastewater or biomass components by employing suitable photocatalysts are some possible ways to improve the energy efficiency, and continuous research in the above directions is highly desirable.

[a] Department of Chemistry, St. John's College (Affiliated to University of Kerala), Anchal, Kerala – 691306, India. E-mail: thomasm74@gmail.com

[b] Catalysis and Inorganic Chemistry Division, CSIR – National Chemical Laboratory, Dr Homi Bhabha Road, Pune 411 008, India. E-mail: cs.gopinath@ncl.res.in

[c] Academy of Scientific and Innovative Research (AcSIR), Ghaziabad 201002, India

Sunesh S. Mani

Sunesh S Mani completed his Master's Degree in Chemistry from the University of Kerala, Trivandrum. He is currently working as a PhD student under the supervision of Dr Thomas Mathew, Department of Chemistry, St. John's College, Anchal, affiliated to the University of Kerala, Trivandrum. His primary research interest is the development of nanomaterials for photocatalytic applications.

Sivaraj Rajendran

Sivaraj Rajendran received his Bachelor's Degree and Master's Degree in Chemistry from the University of Kerala, Trivandrum. He is presently a PhD student in the Department of Chemistry, St. John's College, Anchal, affiliated to University of Kerala, Trivandrum under the supervision of Dr Thomas Mathew. His research interest mainly focuses on the design of transition metal-based nanomaterials for photocatalytic and electrocatalytic applications.

1. Introduction

The steadily increasing demand for energy due to population growth and industrialisation poses a serious concern owing to the depletion of fossil fuels (oil, gas and coal), which account for >85% of energy production and currently the major source of energy.[1,2] Besides the general consensus on limited fossil fuel reserves, the combustion of fossil fuels leads to the emission of CO_2 and other harmful gases, which is a major issue resulting in an almost irreversible change in the atmosphere and thus drastic climate changes. In this case, carbon-free hydrogen production *via* water splitting, with and without a sacrificial agent, in the presence of a semiconductor utilizing solar energy is a renewable process and is considered a promising alternative for an economically and socially sustainable future to meet the increasing energy demand.[3] Given that the overall water splitting reaction for H_2 production is an uphill reaction with a positive Gibbs free energy of 238 kJ mol^{-1}, a photocatalyst that can efficiently harvest solar radiation is essential to make the reaction process energetically and economically feasible.[2] Accordingly, different semiconductor materials, such as TiO_2, Cu_2O, Co_3O_4, CdS, and $ZnIn_2S_4$, have been examined to evaluate their potential as photocatalytic materials in the water splitting reaction to produce hydrogen.[4] Recently, poly(heptazine imide) ionic carbon nitrides are another emerging class of photocatalytic materials applied for hydrogen evolution.[5] Among the various photocatalytic materials, TiO_2 has been an extensively studied semiconductor material due to its several advantages, such as availability, low cost, interesting physico-chemical properties, non-toxicity, environmentally friendly nature, feasible synthesis at low temperatures, amenability to integration with different materials, and high chemical and photostability.[6]

Since the potential of TiO_2 for the photolysis of water was revealed by Fujishima and Honda for the first time in 1972,[6] its performance has been widely explored for a variety of applications, such as photocatalytic degradation of pollutants,[7] supercapacitors,[8] solar cells,[9] carbon dioxide reduction,[10] lithium-ion batteries,[11] biomedical devices,[12] self-cleaning,[13] and water splitting.[14] However, the wide bandgap (3.2 eV) of TiO_2 restricts its light-harvesting ability to mainly the UV region (which is ∼5% of sunlight), and the fast recombination of photo-generated electron–hole pairs in bare TiO_2 limits its photocatalytic functionality.[6] Thus, to overcome the above-mentioned inherent drawbacks of TiO_2 and enhance its photocatalytic performance for solar H_2 production, significant efforts have been devoted to designing catalysts, such as doping with metals and non-metals,[15,16] dye sensitization,[17] use of noble metals (Pt, Pd, Au and Ag) as a co-catalyst,[18] engineering the band structure to match particular energy levels,[19] and fabrication of semiconductor heterojunction and/or Schottky junctions.[20]

In the past few years, several excellent review articles have been published on photocatalytic water splitting for hydrogen production, which are based on different catalyst systems including semiconductor-based catalyst systems,[21,22] metal-free photocatalysts,[23] spinel materials,[24] ionic carbon nitride,[25–28] carbon-based materials,[29] transition metal complexes,[30] and TiO_2-based semiconductor materials.[31–36] Also, although there are few reviews available on TiO_2-based photocatalysts for solar hydrogen production,[31–36] they emphasized the general aspects of photocatalytic H_2 production. Thus,

Thomas Mathew

Thomas Mathew completed his PhD at NCL, Pune and received his degree from the University of Pune in 2003. He gained Postdoctoral experience from AIST, Osaka, Japan (2003–2005), Academia Sinica, Taiwan (2005–2006) and as a JSPS Fellow at the University of Tokyo, Japan (2006–2008), 3 years of R&D experience at Toyota Central R&D Labs, Japan (2008–2011), and 2 years teaching experience in BTech and MTech Nanotechnology at Noorul Islam University, India (2011–2013). He also received an HRSMC Fellowship from The Netherlands to perform experiments on CO_2 utilization at the University of Amsterdam, The Netherlands (02/2022–04/2022). He has been an Assistant Professor since 2013 at St. John's College, India. He has published more than 30 research articles and 2 patents. He is actively involved in teaching chemistry and interdisciplinary topics at the graduate and post-graduate levels. His research interest includes heterogeneous catalysis, photocatalysis, electrocatalytic water splitting, steam reforming, CO_2 utilization and RWGS reaction, and development of novel functional materials.

Chinnakonda S. Gopinath

Dr Chinnakonda S. Gopinath (Gopi) completed his PhD in 1993 at IIT, Madras. After two post-doc stints (AvH Fellowship at Forschungszentrum Karlsruhe (1995–97), and PDF at the University of California at Riverside (1997–2000), he joined CSIR – National Chemical Laboratory (CSIR-NCL), Pune in 2000 as a Scientist. Currently, he is an Outstanding Scientist at CSIR-NCL, and also leading the Hydrogen Technology program across CSIR laboratories). He has been an elected Fellow of the Indian Academy of Sciences since 2012. Gopi is a visiting CNRS Researcher in the University of Lille 1. Thus far, he has published 245 research articles with an h-index of 61 and 12 patents. His research interests include heterogeneous catalysis, surface science under operando conditions, artificial photosynthesis, solar water splitting, electrocatalytic conversion of CO_2 and biomass, and development of novel materials. He is also interested in taking the artificial photosynthesis process from the laboratory level to the market.

readers interested in the above-mentioned aspects can refer those references. In contrast, the present review emphasizes the structure–activity correlation and how material integration is beneficial for tuning the activity of photocatalysts. The various critical changes in the physico-chemical and electronic properties of TiO_2-based materials fabricated by integrating TiO_2 with a variety of dopants and/or materials and its structure–activity relation for solar hydrogen production are addressed in detail. Also, the efficient and concurrent utilization of both photogenerated holes and electrons to improve the photocatalytic efficiency of materials is discussed. Furthermore, we discuss the importance of fabricating photocatalysts in thin film form and performing solar hydrogen production in different reactor set-ups for enhancing the photocatalytic performance of materials and their scalability.

A Scopus-based survey was performed using the following three sets of keywords to determine the number of publications related to TiO_2-based photocatalysts for water splitting, as follows: (i) TiO_2 photocatalysts and hydrogen production, (ii) TiO_2 photocatalysts and water splitting, and (iii) TiO_2-based photocatalysts, and hydrogen production and water splitting. This survey revealed that the articles published in this area have been steadily increasing in the past ten years and the result is shown in Fig. 1. As shown in Fig. 1, an increase in the number of articles on TiO_2-based photocatalysts for H_2 production appeared after 2017, highlighting the importance of sustainable hydrogen production from renewable sources and the worldwide focus on it.

Several variations and advances have been made in the past decade, especially regarding TiO_2-based semiconductor photocatalysts for solar hydrogen production using water as the main hydrogen source. Therefore, in this review, we comprehensively summarize and highlight the recent progress in the design and structure–activity relation of TiO_2-based photocatalysts towards
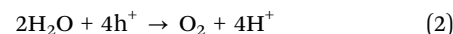
solar hydrogen production with water as the main hydrogen source, where the works employing sacrificial agents are also included to a significant extent. Initially, we provide the fundamental aspects of integrating different materials with TiO_2, such as noble metals, non-noble metals, metal oxides/sulphides/selenides, and low band-gap semiconductors and their structure–activity correlation is highlighted to understand the mechanistic aspects and the entire progress in the field of photocatalytic hydrogen production. Also, the role of TiO_2-based photocatalysts is specifically reviewed based on the effects of various factors including preparation methods, morphology, crystallographic facet-dependent activity, catalyst loading, and dopant concentration. Subsequently, we discuss the importance of engineering strategies, such as the importance of fabricating photocatalysts in thin film form to overcome the drawbacks of TiO_2 in powder form, resulting in improved photoactivity and scalability. Finally, the major challenges and an outlook on the future strategies in this research field are discussed from the viewpoint of the structure–activity relation of various TiO_2-based photocatalysts.

2. TiO_2-based photocatalytic water splitting processes

The photocatalytic splitting of water to H_2 and O_2 on the surface of TiO_2-based semiconductors proceeds through a redox reaction process, as described in eqn (1)–(3).[37]

$$TiO_2 + h\nu \rightarrow e_{(CB\text{-}TiO_2)}^- + h_{(VB\text{-}TiO_2)}^+ \quad (1)$$

$$2H_2O + 4h^+ \rightarrow O_2 + 4H^+ \quad (2)$$

$$4H^+ + 4e^- \rightarrow 2H_2 \quad (3)$$

These redox reactions are accomplished through three critical processes, as follows:[21] (i) absorption of light by a photocatalyst, forming free exciton (e^-–h^+) pairs, (ii) separation of the photogenerated exciton pairs into electrons and holes, followed by their migration to the catalyst surface, and (iii) conversion of water

Fig. 1 Scopus data-based survey (conducted on February 29, 2024) indicating the number of publications in the area of TiO_2-based photocatalytic water splitting for H_2 production, with three different sets of keywords, as explained in the text. (i) TiO_2, photocatalyst and hydrogen production; (ii) TiO_2, photocatalyst and water splitting, and (iii) TiO_2, photocatalyst and hydrogen production through water splitting.

Fig. 2 Flowchart illustrating the fundamental and critical processes involved in semiconductor based photocatalytic water splitting processes.

molecules into hydrogen and oxygen on the catalyst surface by utilizing the photogenerated electrons in the conduction band for reducing protons to H_2 molecules and holes in the valence band for oxidizing water to O_2 molecules. A flowchart illustrating the various fundamental and critical steps involved in the TiO_2-based photocatalytic water splitting process is shown in Fig. 2.

The bandgap and band position of the photocatalyst,[3] the ability of the photocatalyst in enhancing the charge (electron–hole pair) separation and charge diffusion to the redox sites,[38–40] presence of sacrificial reagents,[41] *etc.* are crucial factors that determine the efficiency of solar hydrogen production. The conversion efficiency of solar energy into hydrogen can be calculated by the apparent quantum yield (AQY) according to eqn (4).[42]

$$AQY = 2 \times \frac{\text{Number of hydrogen molecules}}{\text{Number of photons}} \times 100 \qquad (4)$$

3. TiO₂-based water splitting photocatalysts

In the past few decades, significant efforts have been devoted to enhancing the activity of TiO_2-based photocatalysts by modifying the band gap, electron–hole separation and charge transfer characteristics of TiO_2 by integrating it with different components.[42–46] The different types of components used to fabricate electronically integrated TiO_2-based photocatalysts include non-metal dopants (S, N, F, and C),[15,45,46] metal nanoparticles,[47–53] low bandgap metallic oxides (Cu_2O, Fe_2O_3, $CeO_{2−x}$, NiO, Co_2O_3, SiO_2, and ZnO),[6,54–61] metal sulphides (CdS, ZnS, MoS_2, FeS_2, SnS_2, *etc.*),[44,62–65] carbonaceous materials (carbon nanotubes, graphene, reduced graphene oxide (rGO),[66–71] graphitic carbon nitride (g-C_3N_4),[72,73] and dye sensitizers).[74,75] The integration of the above-mentioned components with TiO_2 in the optimum concentration can modify the band gap and electronic structure of pristine TiO_2, resulting in improved photocatalytic activity for H_2 production.[38,39] A schematic representation of the various components used to improve the photocatalytic efficiency of TiO_2 is provided in Fig. 3.

3.1. Metal nanoparticles

The integration of TiO_2 with metal nanoparticles is one of the effective strategies to enhance its electron–hole separation by forming metal–semiconductor Schottky junctions with improved charge transfer efficiency.[76] Due to the difference in the Fermi energy levels of metals and TiO_2, when they come into contact, photoexcited electrons are transferred from TiO_2 to the metal until their Fermi energy levels are equilibrated. The potential of metal nanoparticles as a co-catalyst relies on the ease of electron transfer from the conduction band of TiO_2 to the Fermi level of the metallic surface *via* a Schottky junction. The Schottky junction is formed due to the charge difference between the metal nanoparticles (excess negative charge) and TiO_2 surface (excess positive charge), acting as an effective trap for capturing electrons, which can inhibit the recombination of electrons and holes.[50,77,78]

Fig. 3 Schematic representation of different types of chemical components used to improve the photocatalytic efficiency of TiO_2.

Noble metals including Ru,[79] Rh,[80] Pd,[44,48,81] Au,[49,82–84] Ag,[85–87] and Pt[50,88–90] are widely used as a co-catalyst with TiO_2 in photocatalytic hydrogen production due to their unique properties such as formation of a Schottky barrier,[43,91] efficient interfacial electron transfer, photostability, ability to show surface plasmon resonance,[92] formation of impurity energy levels,[79] and oxygen vacancies.[80] There are two types of noble metals, plasmonic (Ag and Au) and non-plasmonic (Pt, Pd, Ru, and Rh).[48,76] In this case, a Schottky barrier is more critical for non-plasmonic metals such as Pt and Pd, which functions as an effective electron trap, imparting a high density of states to the Fermi level and facilitating charge separation and utilization. For example, non-plasmonic noble metals are not capable of exhibiting visible light absorption; however, they show very high cocatalyst activity.[66,76] Noble metals such as Au and Ag on the surface of TiO_2 increase the photon absorption in the visible region through the localised surface plasmon resonance (LSPR) effect.[93,94] The surface plasmon resonance (SPR) effect increases the production of hot electrons at the interface between the metal and TiO_2. Given that the SPR level of the metal is higher than the conduction band of TiO_2, electrons are transferred from the SPR level of the metal to the conduction band of TiO_2. At the same time, the Schottky barrier can prevent the back transfer of electrons to metal nanoparticles.[49] The formation of an intermediate energy level enables charge separation in Ru and extends the light absorption to the visible region,[79] whereas Rh induces the generation of oxygen vacancies in TiO_2, which allows the withdrawal of electrons from the metal, leading to an enhancement in hydrogen production activity.[80] A schematic illustration of the LSPR effect occurring on the surface of a plasmonic metal nanoparticle and H_2 production augmented by electron transfer *via* the Schottky barrier at the interface

between a metal semiconductor, such as Au nanoparticle, is shown in Fig. 4(a and b).

Although noble metals are highly efficient as co-catalysts for photocatalytic hydrogen generation, their high cost and low abundance limit their application, leading to the investigation of earth abundant and cheap non-noble metals co-catalysts.[95–97] Non-noble metal nanoparticles such as Cu and Ni as co-catalysts with TiO_2 have been found to be highly effective in enhancing the rate of hydrogen production in the water splitting reaction.[16,98–102] Heterogeneous surface-distributed non-noble metal nanoparticles on TiO_2 increase charge separation and facilitate charge transfer.[103] Copper is one of the most studied non-noble metal cocatalysts for solar hydrogen evolution because of its low cost, high conductivity, capability to show SPR effect, *etc.* The presence of metallic copper substantially changes the electronic structure of TiO_2 because of the formation of structural defects or energetic electron trap centres, which prevents electron–hole recombination.[95,98,104] Nickel is another attractive non-noble metal co-catalyst because of its high work function, availability and low cost. The high work function of Ni is favourable for preventing the migration of electrons back into the conduction band of TiO_2 in Ni/TiO_2.[105] Metallic Ni nanoparticles dispersed on TiO_2 as small-sized clusters resulted in an improved photocatalytic hydrogen evolution rate.[105] A schematic description of the properties related to various metal nanoparticles employed for fabricating metal-integrated TiO_2 photocatalyst systems for photocatalytic H_2 production is provided in Fig. 5.

Fig. 5 Schematic representation of various noble metals used for improving the photocatalytic hydrogen evolution activity of TiO_2.

3.2. Bimetallic co-catalysts

Compared to single metallic components, bimetallic cocatalysts provide more active sites for H_2 production. The combined effect and the possible synergistic interaction between the two components in a bimetallic system effectively improve the charge separation and charge transfer, where when one of the bimetallic component is SPR active, it also enhances the light absorption capability.[18,99] For example, Cu/Ag bimetallic quantum dots on TiO_2 nanotubes were shown to be beneficial for solar hydrogen generation, possessing the advantage of the SPR effect of Cu and Ag and co-catalyst capability of Cu.[99] A schematic representation of the synthesis of the bimetallic $Cu/Ag@TiO_2$ nanocomposite and its charge transfer mechanism is provided in Fig. 6.

Similarly, NiCu alloy was also found to enhance the solar hydrogen production with a quasi-artificial leaf device (QuAL) fabricated using Mn-doped CdS integrated with mesoporous TiO_2.[106] Mn-doping in CdS was shown to enhance the visible light absorption to a longer wavelength compared to virgin CdS. In the presence of the NiCu-alloy co-catalyst, the QuAL device with an area of 1 cm^2 was demonstrated to produce 10.5 mL h^{-1} of H_2 with a power conversion efficiency of 4.8%. Another interesting aspect of this QuAL device is the increase in the visible light absorption efficiency due to different-size integrated Mn-CdS, which exhibited a wide range of band-gap values due to the different QD sizes. The fluorescence is emitted from the smaller QDs and apparently absorbed by the significantly larger QDs or the same Mn-CdS nanoparticles.
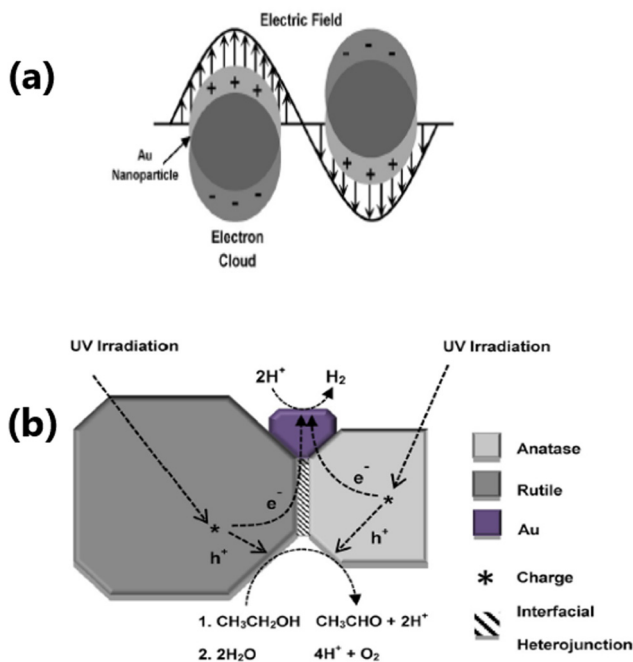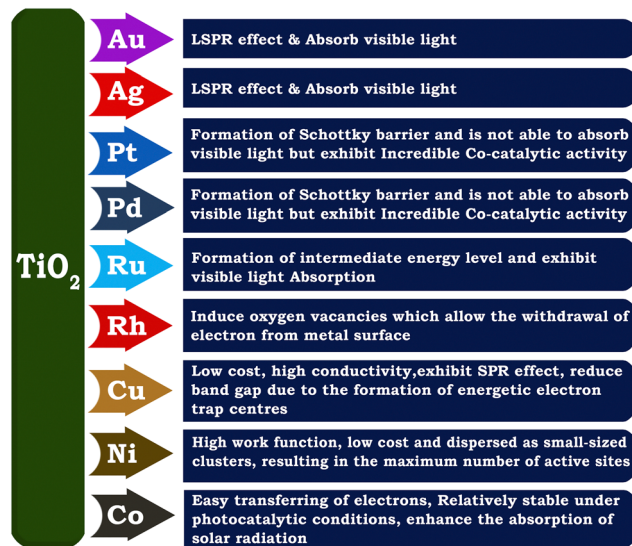

Fig. 4 (a) Schematic representation of LSPR effect showing the oscillation of an electric field of incident light at the resonance frequency on the surface of an Au nanoparticle. (b) Schematic diagram of the proposed mechanism for photocatalytic H_2 production from ethanol/water mixtures over Au/P25 TiO_2. Reproduced with permission from ref. 92. Copyright©2015, Wiley-VCH.

3.3. Non-metal doping

Doping TiO_2 using non-metals such as S,[45] C,[15] F,[46] and N[107] leads to the lowering of its bandgap and is an effective approach to enhance its visible light absorption capability and solar hydrogen evolution.[15,108] The addition of non-metal
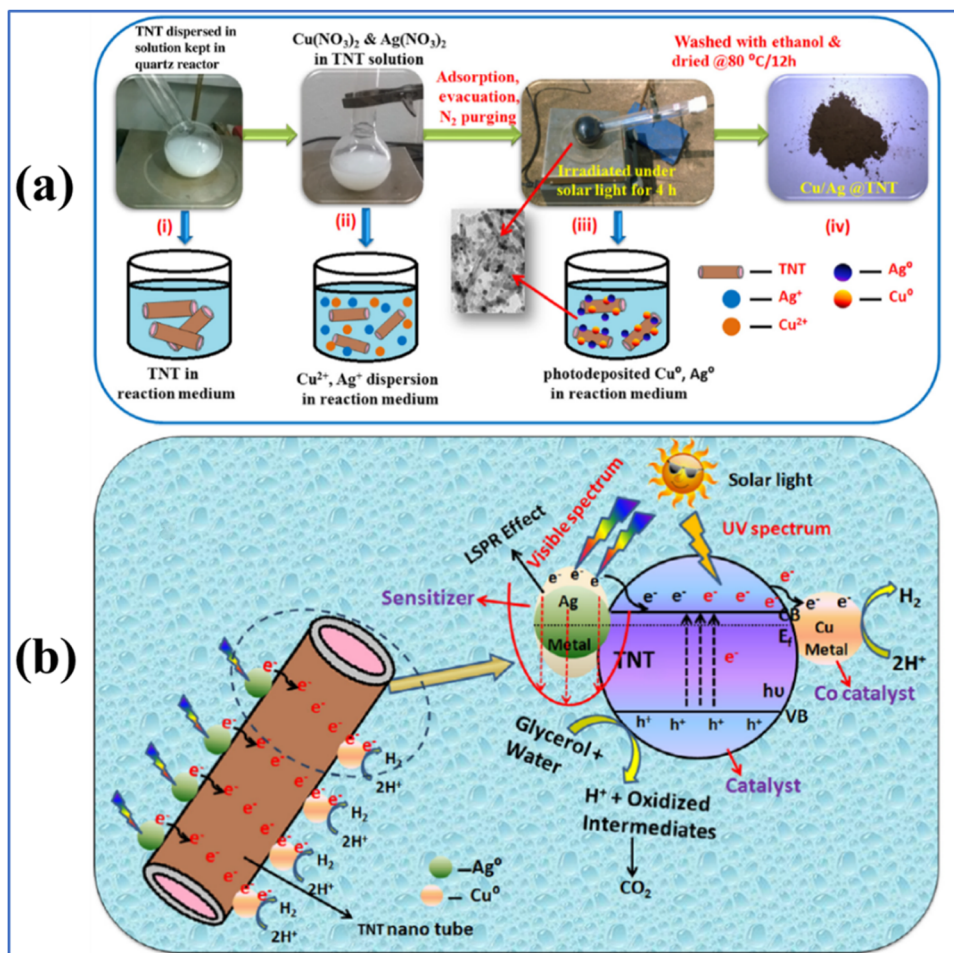
Fig. 6 (a) Schematic synthesis of Cu/Ag bimetallic deposition on titanium nanotubes (TNTs) and (b) charge separation and hydrogen evolution mechanism of as-synthesized Cu/Ag@TiO_2. Reproduced with permission from ref. 99. Copyright©2017, Elsevier Ltd.

dopants in the TiO_2 matrix may generate structural defects in the material, impurity energy level formation, and hence narrowing of the band gap, and also beneficial for overcoming the disadvantages such as carrier trapping and thermal instability that are often encountered with metal nanoparticles.[109–112] Nitrogen is one of the most studied anion dopant because of several advantageous aspects, such as its similar atomic size with oxygen, formation of metastable energy states and considerable overlap of the N 2p and O 2p states, resulting in bandgap narrowing and smooth excitation of electrons between the valence band and conduction band.[113,114] Fig. 7 demonstrates that in comparison to pure TiO_2, the optical properties, valence band characteristics, and band positions of N-doped TiO_2 samples are modified.[115] Further, N-doped samples exhibited an increased in charge separation and charge carrier density compared to pure TiO_2.

3.4. Integration with low band gap semiconductors

The formation of TiO_2-based composites with semiconductors having a low band gap is another efficient strategy for enhancing the rate of photocatalytic hydrogen production. Low band gap semiconductors include both metal oxides and metal chalcogenides. Based on the band position of TiO_2, semiconductors can be classified into two types, *i.e.*, semiconductor having a more negative CB position than TiO_2 (*e.g.*, Cu_2O,[6,116] CuO,[117–119] CeO_2,[55] ZnO,[59] $CuInS_2$,[120] CdS,[62,121,122] and SnS_2[65]), and semiconductor having less negative CB positions than TiO_2 (*e.g.*, $NiSe$,[20] FeS_2,[64] Cu_2S,[6] and MoS_2[63]). A plot of the band positions of TiO_2 and various semiconductors against their redox potentials is depicted in Fig. 8.

The electron hole separation and electron transfer process through the formation of a heterojunction with a low band gap semiconductor depend on the band position of both TiO_2 and the supporting semiconductor. If the CB edge potential of the supporting semiconductor is more negative than that of TiO_2, the photogenerated electrons in the conduction band of the semiconductor usually transfer to the lower-lying conduction band of TiO_2.[54,55,123] In contrast, the CB edge potential of the supporting semiconductor is less negative than that of TiO_2, and the electrons from the conduction band of TiO_2 will be transferred to the lower-lying conduction band of the supporting semiconductor.[20,63,124,125]

3.4.1. Metal oxide semiconductors. Numerous semiconductor metal oxides including ZnO,[59] CeO_2,[55] WO_3,[126] $SrTiO_3$,[127] Y_2O_3,[124] CoO,[128,129] NiO,[56,123,128] Cu_xO,[6,117,130] Ag_2O,[131,132] and Fe_2O_3[54] are
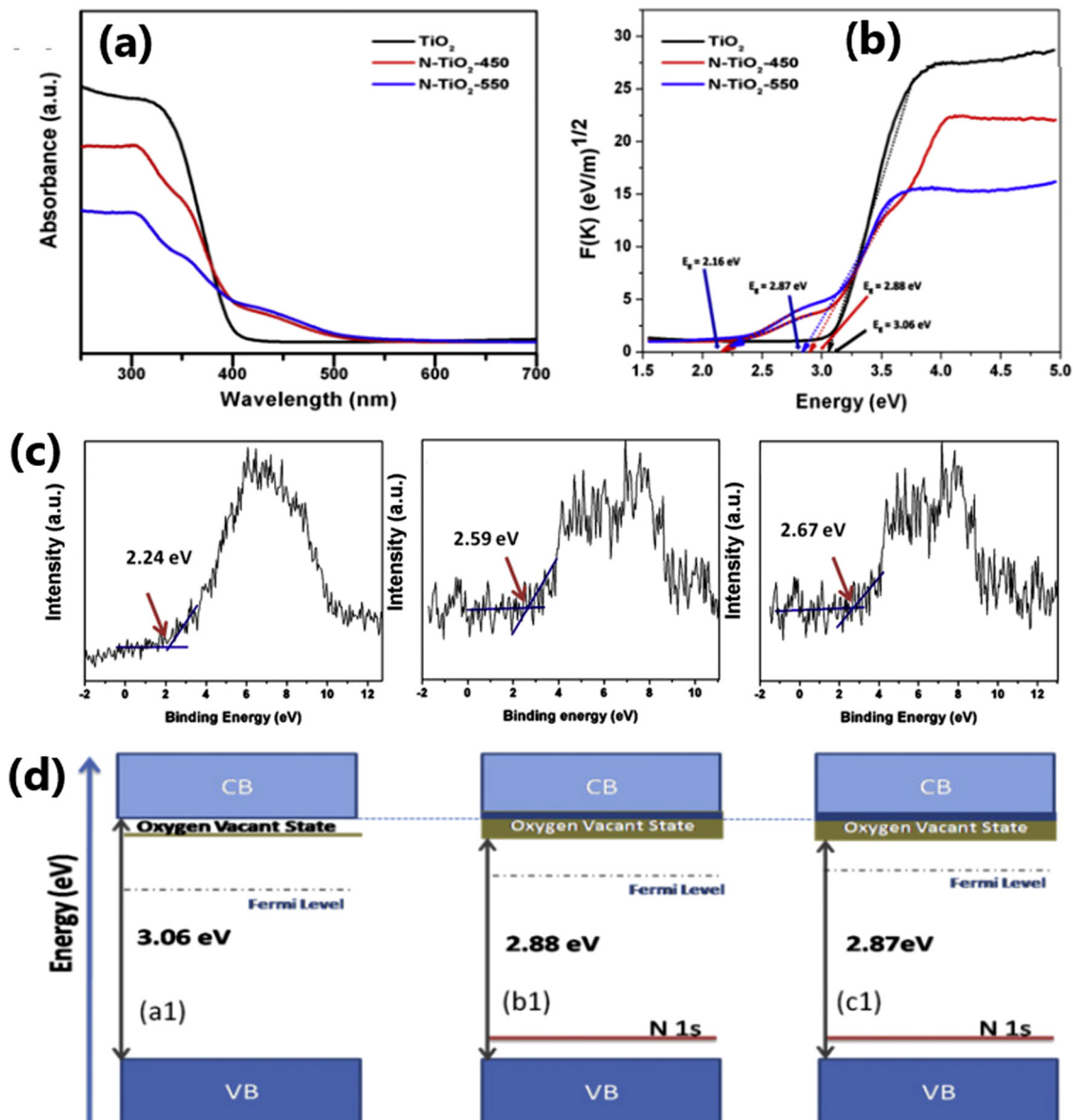
Fig. 7 (a) UV-vis absorbance spectra and (b) Tauc plot obtained from the reflectance spectra and (c) valence band edge analysis of TiO_2, $N-TiO_2$-450, $N-TiO_2$-550. (d) Proposed band diagrams of TiO_2 and N-doped TiO_2 catalysts. Reproduced with permission from ref. 115. Copyright©2016, Elsevier Ltd.

Fig. 8 Plot of band positions of semiconductors against redox potential at pH = 7.

Fig. 9 Schematic representation of various metal oxides used for improving the photocatalytic hydrogen evolution activity of TiO_2.

have been employed for the fabrication of stable and low-cost heterojunction structures with TiO_2. These composites with reduced band gaps have been found to be very effective for electron–hole separation and charge transfer,[63,131,133] and hence promising alternatives to the very expensive noble metal-based photocatalyst systems. The p–n junction formed at the interface between the n-type TiO_2 semiconductor and the p-type semiconductors such as α-Fe_2O_3, CoO, NiO and Cu_xO enhances the rate of photocatalytic H_2 production due to the appropriate band position for water reduction, enhanced charge carrier lifetime and charge transfer rate, and ability to expand its absorption to the visible region.[54,56,123,130,134] A schematic description of the properties related to various metal oxide nanoparticles employed for the fabrication of stable TiO_2 heterojunction photocatalysts for photocatalytic H_2 production is provided in Fig. 9.

The activity of TiO_2 can be further improved by surface modification with Ni (metal) and P (nonmetal), resulting in more effective heterojunctions.[55] For example, after surface decoration with Ni–P, the CeO_2–TiO_2 photocatalyst became an effective photocatalyst for hydrogen evolution due to the lowering of its bandgap to 2.4 eV and powerful electron–hole separation.[55] In this photocatalyst, Ni–P acts as a bridge for electron transportation. Also, SiO_2 is an interesting substrate used for dispersing and maintaining the active phase, imparting thermal stability and improving the surface area of TiO_2-based photocatalysts.[58] For example, the pore channels of SiO_2 were successfully utilized for anchoring TiO_2 quantum dots (TiO_2-QDs) in a highly dispersed state on the surface of silica via the in situ hydrolysis of Ti-alkoxide.[58] The anchoring effect between TiO_2-QDs and the pore-wall of SiO_2 foam provided extra stability to TiO_2-QDs, which helped in maintaining TiO_2-QDs in the anatase phase without undergoing any phase transformation and particle growth even after exposure to high temperature of up to 1000 °C.

NiO is a p-type semiconductor with a bandgap of 3.5 eV, which possesses high charge carrier concentration and high mobility of charge carriers. It can form an efficient p–n heterojunction with anatase TiO_2, which facilitates the red shifting of the bandgap energy of the NiO/TiO_2 heterostructure.[123] The internal electric field developed at the interface of the NiO/anatase TiO_2 p–n heterojunctions facilitates the dissociation efficiency of photogenerated electron–hole pairs and enhances the photocatalytic efficiency. For example, mesoporous heterostructure of 1 wt% NiO on anatase TiO_2 nanoparticulate photocatalyst showed an H_2 production rate of 2693 μmol h^{-1} g^{-1} by methanol photo-reforming, which is higher than that of pure anatase TiO_2 and commercial P25.

3.4.2. Transition metal chalcogenides. The potential of low band gap transition metal chalcogenides, such as molybdenum sulphide (MoS_2),[63] cadmium sulphide (CdS),[121] tungsten sulphide (WS),[125] nickel sulphide(NiS),[135] copper sulphide (Cu_2S),[6] cadmium selenide(CdSe),[136] and $CuInS_2$,[120] in heterojunctions with TiO_2 has been explored for H_2 production by water splitting reaction. The favourable photocatalytic properties of these composite structures, such as remarkable light absorption in the visible region (e.g., TiO_2/MoS_2),[137] excellent charge carrier separation and charge transfer due to their intimate and large contact interface, large surface area with increased number of active sites (e.g., TiO_2/CdS), feasible reduction potential (TiO_2/Cu_2S),[6] large optical absorption coefficient (e.g., TiO_2/FeS_2),[64] excellent chemical stability in acid or neutral solution and thermal stability in air (e.g., TiO_2/SnS_2)[65] endow these materials with high photocatalytic activity and H_2 production rate.[6,64,65,138,139] Guo et al. demonstrated that non-metal plasmonic MoS_2@TiO_2 heterostructures with broad spectral response ranging from the near UV-visible to near IR region exhibited enhanced H_2 production activity.[139] The MoS_2@TiO_2 system was fabricated by a series of reactions involving anodization, physical vapor deposition (VD), and chemical vapor deposition (CVD) processes (Fig. 10a). To gain deep insight into this non-metal plasmonic system, structural and textural analyses, FEM simulation and DFT calculations were also performed (Fig. 10b–i) and it was found that the uniform heterostructure with surface plasmon resonance is responsible for the charge transfer and charge carrier separation process. In another example, the HRTEM images of an FeS_2–TiO_2 composite (Fig. 11b) demonstrated the intimate junction between the (210) facet of FeS_2 and abundantly available (101) facets of TiO_2; consequently, the photocatalytic H_2 production rate shown by FeS_2–TiO_2 was much higher than that of both FeS_2 and TiO_2 (Fig. 11c) due to the efficient electron–hole separation mechanism of the composite material, as illustrated in Fig. 11a.[64] There are some novel chalcogenides that act as excellent photocatalytic systems.[4] For example, the excellent photocatalytic activity of $ZnIn_2S_4$ was reported in the literature.[4] Its layered structure provided sufficient active sites for photocatalytic reactions, thus enhancing its overall catalytic performance. Additionally, the long-term durability study of this catalyst in repeated catalytic cycles revealed that $ZnIn_2S_4$ exhibits strong photochemical stability.[4]
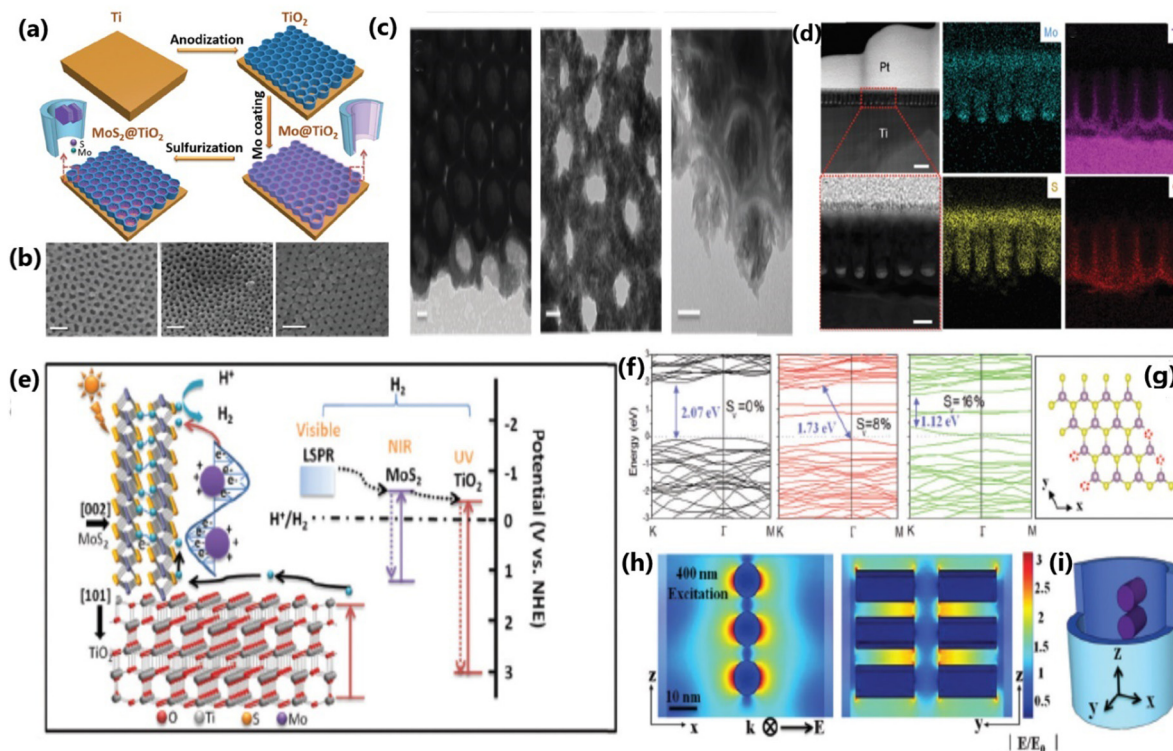
Fig. 10 (a) Schematic illustration of the assembly process of the MoS$_2$@TiO$_2$ heterostructure. (b) SEM pictures of MoS$_2$(10)@TiO$_2$, MoS$_2$(20)@TiO$_2$ and MoS$_2$(30)@TiO$_2$, respectively (scale bar: 100 nm). (c) TEM and HRTEM images of MoS$_2$(10)@TiO$_2$ and MoS$_2$(20)@TiO$_2$ (scale bar: 20 nm). (d) Cross-sectional HAADF-STEM images and EDS elemental mapping of the MoS$_2$@TiO$_2$ heterostructure (first row, scale bar: 200 nm, and second row, scale bar: 50 nm). (e) Schematic diagram of the energy band structure, plasmonic resonance and electron transfer pathway in the MoS$_2$@TiO$_2$ heterojunction. (f) Band structure of monolayer 2H-MoS$_2$ with 0%, 8% and 16% S-vacancies, with the valence band maximum and conduction band minimum both at the K point. (g) Model used for band gap computation *via* DFT. (h) FEM simulation of the near-field electric field distribution inside MoS$_2$@TiO$_2$ heterostructures excited by a 400 nm laser and (i) 3D-simplified model used for FEM simulation. Reproduced with permission from ref. 139. Copyright ©2018, The Royal Society of Chemistry.

3.5. Carbon-based photocatalytic materials

The combination of TiO$_2$ with carbonaceous materials such as graphene,[70,140] graphene oxide,[66,141,142] carbon nanotubes (CNTs)[67] and graphitic carbon nitride (g-C$_3$N$_4$)[143–146] leads to highly promising heterostructures for photocatalytic hydrogen generation, in addition to mechanical strength. A study[70] reported a rough estimate of the weight ratio of TiO$_2$ to RGO of around 10^5–10^6; nonetheless, the RGO layers seem to be intact without any faults. These composite materials were effective in preventing the agglomeration of metal nanoparticles and displayed good light absorption capacity and electron–hole separation.[147] The two-dimensional (2D) carbonaceous materials reported in the literature to enhance the rate of photocatalytic H$_2$ production of TiO$_2$ nanocomposites include graphene,[148] reduced graphene oxide,[149] and g-C$_3$N$_4$.[68,144,150,151] The excellent physical, chemical and photocatalytic properties of these TiO$_2$-2D carbonaceous materials, such as high specific surface area, high mechanical and chemical stability, outstanding visible light absorption ability, high electrical conductivity and charge carrier mobility, ability to shuttle charges between the composite material and regain its sp^2 hybridised structure, spatial charge separation of electron–hole pairs, reduced band gap and good charge separation make them highly promising photocatalytic materials.[67,68] The enhanced photocatalytic activity and H$_2$ production ability of CNT/TiO$_2$ composite materials are due to the significant electron transport and optical properties of CNT and creation of an intermediate energy level, which help to improve the visible light absorption capacity of the material.[67,68,152] Fig. 12 illustrates the synthesis protocol for fabricating TiO$_2$/g-C$_3$N$_4$ nanosheet composites, detailing their optical absorption properties, morphology, photocatalytic hydrogen evolution mechanism, and valence band characteristics.

3.6. Dye sensitization

Dye sensitization is a simple and effective technique to improve the visible light-harvesting capacity,[17,153] and thereby the photocatalytic hydrogen production activity of materials. Amongst the different dye sensitizers, organometallic complexes[17] and metal-free organic dyes[154] are the most widely used and TiO$_2$ in combination with them display enhanced photocatalytic hydrogen production.[155] During photocatalysis, the electrons from the lowest unoccupied molecular orbital of the sensitized dye are injected into the conduction band of TiO$_2$, leading to the efficient separation of electrons and holes. In comparison with dye-sensitized TiO$_2$, bare TiO$_2$ shows poor solar light conversion
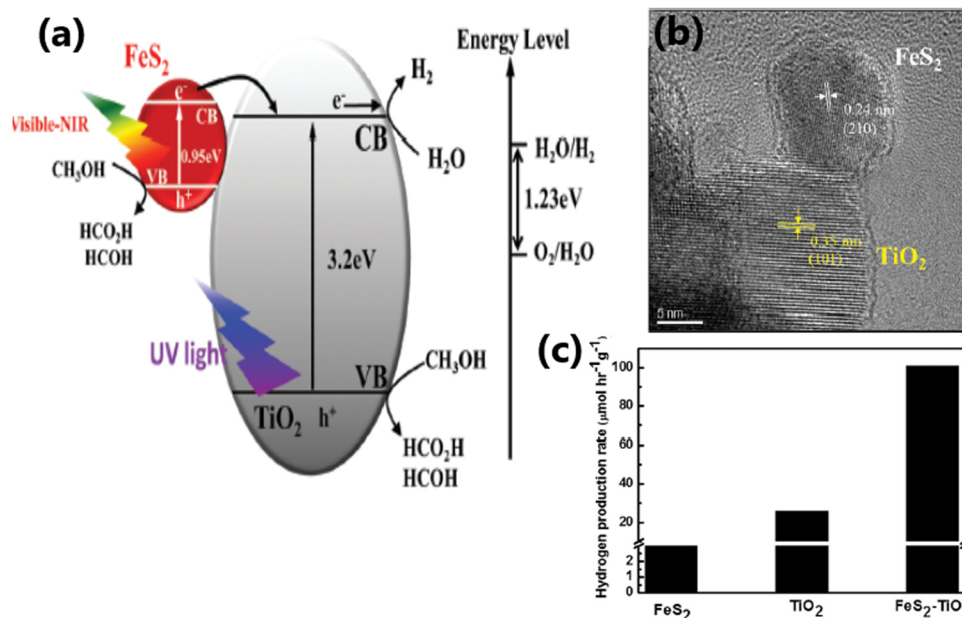
Fig. 11 (a) Schematic illustration of the interfacial charge transfer process in FeS_2–TiO_2 catalyst under UV, visible and near-IR light irradiation. (b) HRTEM image showing the intimate contact between the (210) plane of FeS_2 and the (101) plane of TiO_2 in FeS_2–TiO_2. (c) Rate of hydrogen evolution from TiO_2, FeS_2 and the FeS_2–TiO_2 nanocomposite under a 300 W xenon lamp. Reproduced with permission from ref. 64. Copyright ©2018, the Royal Society of Chemistry.

efficiency.[100] Dyes used for sensitization, especially organic dyes, may degrade with time as a result of exposure to light, changes in temperature, or chemical interactions with the environment. As a result of this deterioration, the overall stability and effectiveness of the photocatalytic system may decrease. In certain cases, the photochemical stability of dyes may be enhanced if the dye and semiconductor are connected by a covalent bond rather than a weak interaction.[156] A diagrammatic illustration of the dye sensitization and the hydrogen evolution mechanism of Eosin

Y-sensitized C-TiO_2 hollow nanoshell system is presented in Fig. 13.[155]

3.7. TiO_2-based ternary composite material

The construction of structurally organized ternary nanocomposites with efficient heterojunctions through their intimate contact is a versatile approach to improve the photocatalytic performance and hydrogen yield of the water splitting reaction. Different types of ternary composite systems with superior
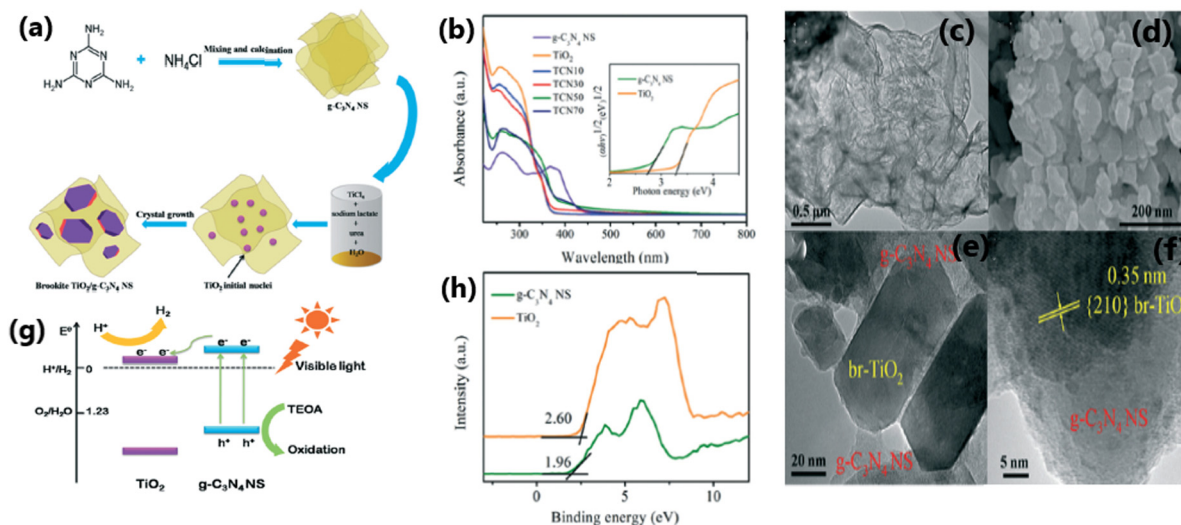
Fig. 12 (a) Schematic illustration of the synthesis of TCN_x composites. (b) UV-vis absorption spectra of TiO_2 and TCN_x composites. SEM images of (c) g-C_3N_4 NS and (d) TCN50. (e) and (f) HRTEM images of TCN50. (g) Proposed mechanism for visible light photocatalytic activities of TCN_x composites. (h) VB XPS of TiO_2 and g-C_3N_4 NS. Reproduced with permission from ref. 151. Copyright ©2017, the Royal Society of Chemistry.
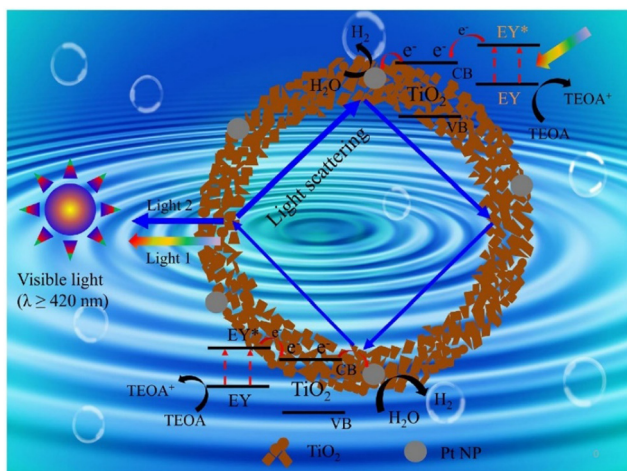
Fig. 13 Mechanism for photocatalytic H_2 evolution over eosin Y-sensitized C-TiO$_2$ hollow nanoshells with Mie resonance. Reproduced with permission from ref. 74. Copyright ©2021, Elsevier Ltd.

Fig. 14 Schematic illustration of the mechanism of photocatalytic hydrogen evolution from an Au–Pd/rGO/TiO$_2$ triple composite, in which an SPR electron from Au is transferred to TiO$_2$ via rGO. Reproduced with permission from ref. 66. Copyright ©2019, ACS.

catalytic performance compared to the corresponding binary composites have been reported in the literature, which include Au–Pd/rGO/TiO$_2$,[66] Au/(TiO$_2$–g-C$_3$N$_4$),[157,158] Pt/Cu/TiO$_2$,[117] GO/TiO$_2$/ZnIn$_2$S$_4$,[142] CuInS$_2$/TiO$_2$/MoS$_2$,[120] CuO–Co$_3$O$_4$/TiO$_2$,[159] Pd–SrIn$_2$O$_4$–TiO$_2$,[160] CuS–TiO$_2$/Pt,[161] and Cu$_2$O/TiO$_2$/Bi$_2$O$_3$.[162] The different hydrogen generation activities reported for the same/similar catalysts from the above-mentioned references suggest that the quality of heterojunctions is different, which may be one of the main reasons for efficient charge separation and migration to the redox sites. For example, the superior activity of the Au/(TiO$_2$-gC$_3$N$_4$) ternary composite is due to the efficient charge separation and enhanced visible light absorption in a wide wavelength range resulting from the SPR effect of Au nanoparticles and the potential to shuttle electrons using g-C$_3$N$_4$.[157,163] The photocatalytic performance of TiO$_2$ can be enormously improved by creating a triple composite CuInS$_2$/TiO$_2$/MoS$_2$, which exhibit a huge absorption range from the UV region to the near-infrared region.[120] On irradiation, the excited electron from CuInS$_2$ is smoothly transferred via TiO$_2$ to MoS$_2$, where the adsorbed proton is reduced to H$_2$.[120] The metal nanoparticles in ternary composites act as an effective co-catalyst and further enhance the rate of hydrogen generation by supplying electrons and active sites.[66,157,160] Fig. 14 shows a schematic illustration of the electron transfer mechanism and photocatalytic H$_2$ production over an Au–Pd/rGO/TiO$_2$ triple composite, wherein the SPR-induced electron is directly transferred from Au to the CB of TiO$_2$ via rGO.[66] Table 1 lists a detailed comparison of the H$_2$ yield and the corresponding experimental conditions for some TiO$_2$-based photocatalysts.

4. Factors influencing solar hydrogen generation activity of TiO$_2$

The performance of a photocatalyst and its photocatalytic hydrogen evolution activity depend on the extent of electron and hole photogeneration 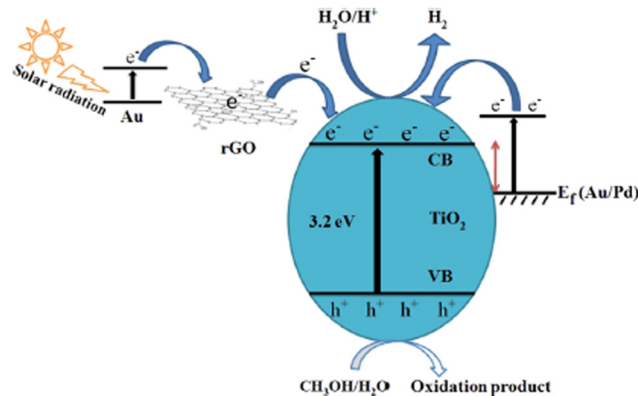and large extent of charge separation, followed by charge transfer to the redox sites for redox reactions to occur.[133] The use of dopants and/or co-catalysts in suitable combination and composition and their synthesis strategy are crucial to obtaining efficient photocatalysts and various material properties, such as morphology, surface area, particle size, and band gap are beneficial for realizing the maximum performance for solar H$_2$ production.[76,123] The critical factors that determine the photocatalytic performance in solar hydrogen evolution on TiO$_2$-based photocatalysts are summarized in Fig. 15.

4.1. Effect of preparation method

The synthesis method largely influences the physical and chemical properties of photocatalysts, which in turn have a huge impact on the rate of solar hydrogen evolution.[67,134,184] Accordingly, numerous new synthesis strategies have been developed in recent years for the fabrication of TiO$_2$-based photocatalysts, which include molten salt method,[172] impregnation method,[67,184] sol–gel (SG) method,[184] chemical adsorption decomposition (CAD),[184] composite precipitation (CP),[184] ionic liquid-assisted hydrothermal method (ILAHM),[134] chemical bath deposition process (CBD),[9] and electrospinning preparation. A schematic representation of some of the most common synthesis strategies of TiO$_2$-based photocatalytic systems reported in the literature is shown in Fig. 16.

Li et al. reported six distinct preparation methods for the fabrication of CuO/TiO$_2$ photocatalysts and evaluated the performance of these differently prepared materials in the photocatalytic hydrogen evolution reaction.[184] As illustrated in Fig. 17, among the methods, including CAD, CP, impregnation (EI, SWI, and SI) and SG, CuO/TiO$_2$ prepared via the CAD method showed the highest rate of hydrogen evolution (3155.7 μmol g^{-1} h^{-1}). The highest activity of the material prepared via CAD is due to the formation of TiO$_2$ in the anatase/rutile mixed-phase. The advantages of anatase/rutile mixed-phase include enhanced electron–hole separation, transfer of electrons from rutile to anatase phase, and formation of catalytic hotspots at the interface of the anatase and rutile phases.

Table 1 Hydrogen yield and experimental conditions associated with various TiO_2-based photocatalytic systems reported in the literature

No.	Material	Experimental conditions	H_2 yield/ mmol h^{-1} g^{-1}	Ref.
		Metal-integrated TiO_2		
1	0.5Rh/TSG (TiO_2 sol–gel)	50 mg of 0.5Rh/TSG photocatalyst in aqueous solution of ethanol (50% v/v, water), UV Pen-Ray Hg lamp ($\lambda = 365$ nm)	7.2246	51
2	Ru 8.0/TiO_2 NBs-400	10 mg of photocatalyst was suspended in 10 mL of water containing 0.1 g of ethylenediamine tetra acetic acid disodium salt (EDTA-2Na), 300 W xenon lamp	25.34	47
3	TiO_2Ag-F	200 mg catalyst in 200 mL of distilled water, 4 mL of methanol, 250 W mercury lamp	0.180 in 4 h	38
4	TiO_2–Au-1% Pt	10 mg of TiO_2–Au photocatalyst into an aqueous methanol solution (120 mL, 25 vol%), 300 W Xe Lamp UV cut-420 nm filter	0.0924	49
5	3 wt% Au/P25 TiO_2	(6.5 mg) was placed in ethanol (15 mL) and Milli-Q water (3.75 mL), 200 W, 365 nm with 6.5 mW cm^2	31.5	92
6	Ag@TiO_2	0.05 g catalyst was suspended in deionized water and methanol mixed solutions (40 mL, 3:1), 300 W xenon lamp	0.5319	164
7	Pd/P25 1 wt% of Pd	Thin film forms of photocatalysts (1 mg) with 25% v/v aqueous methanol solution, direct sunlight 50.2 mW cm^{-2}	104	165
8	Au(2%)@TiO_2	15 mg of photocatalyst was dispersed in 25 mL total volume containing 20% methanol (v/v) in aqueous solution, natural sunlight	3.99 µmol h^{-1} with 100 mg	166
9	The TiO_2–Pd NSs	15 mg photocatalyst was dispersed in 50 mL of methanol/H_2O mixture (20 vol% methanol), 300 W Xe UV lamp and vis-NIR light were used as illumination source, 400 nm cutoff filter 2.7 and 100 mW cm^{-2}	2.80	167
10	Au@TNT	50 mg of photocatalyst was added to 100 mL of methanol-deionized water mixed solution ($V_{MeOH}/V_{H_2O} = 1:10$), Xe lamp ($\lambda > 400$ nm), intensity of incident visible light (400 nm) was 0.1 W cm^{-2}	0.482	168
11	1.5% Ag/TiO_2	20% (v/v) aqueous solution of $Na_2S + Na_2SO_3$, 254 nm wavelength UV light, intensity of light was 4.40 mW cm^{-2}	23.496	112
12	TiO_2–Au 9 wt%	30 mg of catalyst was dispersed in 150 mL of water/methanol mixture with the volume ratio of 9:1, 300 W xenon arc lamp intensity was 380 mW cm^{-2}	12.440	169
13	Pd/TiO_2 nanosheets (0.18 At% Pd NPs)	50 mg of photocatalyst in 50 mL of an aqueous solution containing 20% methanol in volume, 300 W Xe lamp equipped with a cut-off filter i ($\lambda > 420$ nm), light intensity (50 mW cm^{-2})	3.096	170
14	0.1 mol% Ru–TiO_2	0.5 g of fine powder photocatalyst was suspended in 550 mL water and 50 mL methanol, 500 W Hg mid-pressure immersion lamp $\lambda > 320$ nm	3.400	79
15	1 wt% Ag/TiO_2(TiAg-1)	1 mg photocatalyst was dispersed in 1 mL ethanol drop-casted on a thin film, 25% (v/v) methanol/water mixture, direct sunlight	4.59	43
16	TiO_2/Cu	20 mg of TiO_2 and a given amount of metal particles were added to 30 mL, 15 W black light with emission of ~352 nm; 1.0 mW cm^{-2}	0.850 mmol g^{-1} in 3 h	171
17	Cu/Ag@TNT 0.1 M Cu and 0.1 M Ag	5 mg of catalyst was dispersed in 50 mL of 5 vol% glycerol aqueous solution, 300 W Xe lamp with a UV cutoff filter with wavelength of >400 nm	56.167	99
18	TiO_2–Ni-1%	50 mg photocatalyst was added to methanol solution (20 vol%), 300 W Xe lamp	1.433	16
19	Cu(3%)–TiO_2/ErB	5 mg of catalyst in 70 mL water containing 10 vol% triethanolamine, 300 W Xe lamp 0.15 W cm^{-2}	13.4	104
20	0.5 wt% Ni/P25 TiO_2	Photocatalyst (6.5 mg) was placed in the reactor and 20 mL of an aqueous glycerol mixture (10 vol%), 100 W, 365 nm at a distance of 10 cm from the reactor. The photon flux at the sample was 6.5 mW cm^{-2}	26.0	101
21	Ni-a/$TiO_2$0.46 wt%	50 mg of the sample disperses in 100 mL of 10 vol% methanol aqueous solution, 300 W Xe lamp	0.0945 mmol h^{-1} with 50 mg	172
22	TiO_2–NT/Pd–ND	1 mg catalyst in H_2O/MeOH solution (2:1), 300 W Xe lamp, maximum intensity of 203.3 mW cm^{-2} at wavelength of 365 nm	0.143 mmol h^{-1} with 1 mg	173
		TiO_2 with non-metals		
23	15 wt% S-modified TiO_2/β-SiC	0.05 g of catalyst was suspended in 50 mL of an aqueous solution containing 10 vol% of methanol solution, 125 W medium pressure Hg visible lamp was used, 1 M $NaNO_2$ solution as a UV filter under visible light irradiation ($\lambda \geq 400$ nm)	1.254	45
24	N-doped TiO_2 hollow fibres nitrogen up to 5 at% (N-TiO_2)	Photocatalyst sample (0.02 g) was immersed in an aqueous methanol solution (5 mL methanol and 20 mL deionized water), 150 W Xe lamp optical filter, which allowed only wavelengths higher than 420 nm	0.185 µmol g^{-1} in 6 h	108
25	TiO_2/C	5 mg catalyst powder in aqueous solution (10 mL) consisting of triethanolamine (10 vol%), 300 W Xe lamp, cut-off filter ($\lambda > 400$ nm)	57.2 µmol h^{-1} with 5 mg	174
		TiO_2 with metal oxide semiconductor		
26	5 wt% Fe_2O_3/TiO_2	50 mg Fe_2O_3/TiO_2 nanocomposite was suspended with magnetic stirring in 200 mL aqueous solution 10 vol% glycerol, 500 W Xenon lamp with UV cutoff filter ($\lambda > 420$ nm)	1.0 mmol h^{-1} g^{-1}	54
27	Ni–P/CeO_2–TiO_2	0.5 g of the prepared catalyst was directly dispersed in 20 mL deionized water, 1 Sun (1000 mW cm^{-2}) was applied by a solar simulator	1.30 mmol in 5 h with 0.5 g	55
28	Pt/NiO–TiO_2	0.1 g of catalyst was suspended in water + methanol mixtures (33% v/v, 15 ml), 400 nm, $\lambda_{max} = 536$ nm (medium-pressure Hg lamp, 400 W) and UV-vis light source (Hg lamp, 400 W)	0.537 mmol g^{-1} h^{-1}	56
29	TiO_2-QDs/SiO_2	50.0 mg of TiO_2/SiO_2 composite photocatalyst was suspended in 80.0 mL of aqueous solution containing methanol (25.0 vol%), UV-LEDs (3 W, 365 nm)	10.399 mmol g^{-1} h^{-1}	58
30	TiO_2–ZnO-(0.6%)	30 mg catalyst powder was ultrasonically dispersed into 80 mL H_2O, and then 20 mL methanol, 300 W Xe lamp, the light intensity was kept at around 244 mW cm^{-2}	0.3135 mmol h^{-1} with 30 mg	59

Table 1 (continued)

No.	Material	Experimental conditions	H_2 yield/ mmol h^{-1} g^{-1}	Ref.
31	2.82 wt% $Ag_2O \cdot TiO_2$	0.2 g catalyst was suspended in 100 mL glycerol aqueous solution (with 7 vol% of glycerol), 300 W Xe arc lamp (320–780 nm)	336.7 μmol h^{-1} g^{-1}	131
32	1 wt% NiO/anatase TiO_2	(50 mg) and the mixture of methanol/H_2O (1 : 1 v : v, 10 mL), UV-light (Hg vapor light source (LUMATEC SUPERLITE 400))	2.693	123
33	25 wt% of Y_2O_3 in TiO_2	Photocatalyst (10 mg) was dispersed in a 7.5 mL aqueous solution. After sonication, 2.5 mL ethanol was added as a sacrificial reagent, 300 W Xenon/Mercury lamp	1.380 in 2.5 h	124
34	1 wt% Cu/TiO_2	Photocatalyst (2.5 mg) was loaded in the reactor containing 25 mL of a glycerol–water mixture (5 vol% glycerol), 100 W, 365 nm UV light, excitation at ~6.5 mW cm^{-2}	15.32	175
35	2.5-Cu_2O/TiO_2	450 mL aqueous solution, 10 vol% ethylene glycol as a scavenger in reaction solution, 500 W Xe arc lamp bandpass filter (λ = 365 nm with the photon flux of 3.6 mW cm^{-2})	2.048	176
36	TiO_2–(0.1 wt%)CuO	0.1 g of the sample was suspended in 1 M KOH, 300 W xenon lamp	2.715 in 5 h	177
37	Cu_2O/TiO_2	0.1 g of the Cu_2O/TiO_2 photocatalyst was dispersed in 100 mL 10 vol% aqueous methanol, 300 W xenon lamp with or without a bandpass filter (λ > 420 nm)	24.83	178
		TiO_2 with metal chalcogenides		
38	S-doped hetero nanos-tructured TiO_2/Cu_2S	Aqueous solution containing 0.35 M Na_2SO_3 and 0.35 M Na_2S, visible light irradiation conditions (λ > 420 nm)	1.280 with 50 mg	6
39	NiSe/TiO_2	50 mg of the as-prepared photocatalyst powder in 100 mL aqueous solution containing 10 vol% methanol	55.4 μmol h^{-1}	20
40	FeS_2–TiO_2	1 g catalyst (50% aqueous methanol solution), mercury arc lamp (400 W)	0.331	64
41	MoS_2/TiO_2 (0.14 wt%)	50 mg photocatalyst was suspended in 80 mL solution containing 20 mL methanol, four low-power LEDs (3.5 W cm^{-2}, λ = 365 nm)	2.443	125
42	10 mmol NiS/TiO_2 nanosheet films	80 mL 10% ethanol/H_2O (v/v) solution, 500 W Xe lamp	4.31 μmol cm^{-2} in 3 h	135
43	MoS_2/TiO_2	MoS_2@TiO_2 films with a size 7 × 7 mm were submerged in 15 mL of mixed solution made of DI water (seawater) and methanol (8 : 2 by volume), solar light simulator (AM 1.5, 300 W Xe, 100 mW cm^{-2})	580	139
44	0.50 wt% MoS_2, 2D-2D MoS_2/TiO_2	100 mg photocatalyst in 100 mL aqueous solution containing 10% methanol in volume, 300 W Xe-arc lamp	2.145	137
45	2D/1D TiO_2 nanosheet/CdS nanorods	50 mg photocatalyst was suspended in aqueous solution (20 mL lactic acid, 210 mL water), 300 W Xenon arc light source after filtering the UV light with circulating cooling $NaNO_2$ aqueous solution (1 M) to pass only visible light (λ > 400 nm)	128.3	179
		TiO_2 with carbonaceous material		
46	g-C3N4-TiO_2 (1 : 4)	75 mg of photocatalyst was dispersed in 75 mL of aqueous solution containing 10% triethanolamine, 250 W visible light source	1.041	68
47	TiO_2-100-G	Photocatalyst (100 mg) was dispersed in an aqueous solution containing H_2O (80 mL) and CH_3OH (20 mL), 300 W Hg lamp with a wavelength of approximately 365 nm	1.93	180
48	TiO_2/g-C_3N_4	15 mg sample dispersed in 8 mL ethanol and 72 mL H_2O, 150 W Xenon lamp with a cutoff filter (λ > 420 nm)	0.35	181
		TiO_2 with dye sensitization		
49	C-TiO_2 hollow nanoshells with Eosin Y sensitization	Under visible light irradiation (λ > 420 nm)	0.468	74
50	$Ru(dcbpy)_3$/TiO_2	50 mL of solution containing 20 mg of photocatalyst and EDTA (2 mmol L^{-1}), irradiated by a xenon lamp (150 W) with a UV cutoff filter (λ > 400 nm)	94 μmol g^{-1} in 5 h	17
51	Carbazole-based organic dye-sensitized Nafion-coated Pt/TiO_2 system (D1@NPT)	20 mL aqueous suspension containing 10 mg of the photocatalyst and 10 vol% of TEOA as SED, Xenon arc lamp (400 W) was used as a light source	67.9 μmol h^{-1}	154
52	BE-Au(1 wt%)-TiO_2(modified poly(benzothiadiazole) flake denoted as BE)	30 mg catalyst was dispersed in 30 mL 10% vol TEOA aqueous solution, filters (λ = 420, 500 nm, *etc.*) are used	781.2 μmol h^{-1}– 30 mg	182
		TiO_2-ternary composite material		
53	Au–Pd/rGO/TiO_2	25 mg of the catalyst was suspended in 40 mL of an aqueous methanol solution (25% v/v), (300 W xenon arc lamp) with AM 1.5 filter under 1 sun conditions (100 mW cm^{-2})	21.50	66
54	Pt0.5–Au1/TiO_2	(20 mg) of catalyst was added to 30 mL of distilled water and 10 mL methanol, 300 W power AM1.5 (100 mW cm^{-2}) or >400 nm (92 mW cm^{-2}) filter	1.275	76
55	0.5 wt% Pt/0.1 wt% Cu/TiO_2	20 vol% methanol–water, photocatalyst powder (14 mg) was mixed with distilled water (1.2 mL), deposited on 0.85–0.42 mm quartz beads (3 g), xenon arc lamp, 300 W, 40.0 mW cm^{-2} irradiation intensity	27.2	117
56	$CuInS_2$/TiO_2/MoS_2 photocatalyst with 0.6 mmol g^{-1} $CuInS_2$ and 0.5 wt% MoS_2	50 mg photocatalyst was suspended in 250 mL of an aqueous solution containing 0.1 M Na_2S and 0.1 M Na_2SO_3, 300 W Xenon lamp equipped with a UV cutoff filter (λ > 420 nm)	1.034	120
57	rGO/TiO_2/ZIS (2.0 wt% rGO and 50 wt% ZIS)	0.01 g of sample is added into 10 mL of aqueous solution containing 0.35 M of Na_2S and 0.25 M of Na_2SO_3, with a light source (300 W Xe lamp)	0.4623	142
58	0.5 wt% Au/(TiO_2–g-C_3N_4) (95/5)	1 L of Milli-Q water and triethanolamine (TEOA) (1 vol%), solar light	1.750	157

Table 1 (continued)

No.	Material	Experimental conditions	H_2 yield/ mmol h^{-1} g^{-1}	Ref.
59	CuO(1%)–Co$_3$O$_4$ (0.05%)/TiO$_2$	20 mg photocatalyst was suspended in 100 mL of pure water or methanol aqueous solution (30 vol%), 300 W Xe lamp, light intensity of 600 mW cm^{-2}	0.273 with 20 mg	159
60	2 wt% Cu$_2$O/TiO$_2$/Bi$_2$O$_3$	5% glycerol–water solution 0.05 g L^{-1} photocatalyst, natural solar light	6.727 with 50 mg	162
61	Pt(0.02%)Co$_3$.O$_4$(0.005%)(D)/N-TiO$_2$ (PCNT(D))	100 mg of photocatalyst dispersed in 100 mL of an aqueous solution containing methanol (V_{H2O}: V_{MeOH} = 9:1), 300 W Xe lamp and a UV light cutoff filter ($\lambda > 400$ nm) with a light intensity of 380 mW cm^{-2}	197	183

Fig. 15 Schematic representation of the various factors that determine the photocatalytic hydrogen evolution activity of TiO$_2$-based photocatalysts.

Fig. 16 Schematic representation of the various strategies for the synthesis of TiO$_2$-based photocatalyst systems reported in the literature.

A comparison of the activity of the TiO$_2$/CuO nanocomposites prepared via the ILHAM, hydrothermal, sol–gel and ionic liquid co-precipitation methods for photocatalytic H$_2$ production was reported, and this study revealed that the TiO$_2$/CuO nanocomposite produced via ILHAM showed the highest hydrogen evolution activity (8.670 mmol g^{-1} within a period of 2.5 h) under a xenon/mercury lamp using aqueous methanol.[134] The highest activity of the TiO$_2$/CuO nanocomposite obtained by the ILAHM method is attributed to the versatility of this synthesis strategy to control the morphology and other physico-chemical characteristics of the catalyst by utilizing the unique properties of ionic liquids such as thermal stability and low vapor pressure.[134]

A comparison of the photocatalytic activity of mesostructured Ag@TiO$_2$ prepared by the in situ electrospinning method and electrospinning in combination with the photo-deposition approach revealed that Ag@TiO$_2$ nanofibers prepared through the former method displayed a higher H$_2$ yield of 531.9 μmol g^{-1} h^{-1} under one sun conditions with 25% aq. methanol.[164] The high activity of the Ag@TiO$_2$ nanofibers

fabricated via the in situ electrospinning method is attributed to its relatively large BET surface area (39.8 m^2 g^{-1}) and smaller particle size (16.5 nm) than that prepared by the other method.[164]

Xiao et al. developed a new molten salt technique to synthesize atomically dispersed Ni species on TiO$_2$, as illustrated in Fig. 18a for application in photocatalytic water splitting to produce H$_2$, which exhibited 4-times higher activity (94.5 μmol h^{-1} for 50 mg of sample) than Ni/TiO$_2$ prepared by the conventional impregnation method.[172] The experimental and theoretical studies (Fig. 18b–d) revealed that the higher activity of Ni/TiO$_2$ produced by the molten salt technique is due to the fact that it enabled the atomic distribution of Ni ions on TiO$_2$, which favoured the formation of strong Ni–O bond and large number of oxygen vacancies. Consequently, this made the material highly integrated and was beneficial for efficient charge carrier utilization. The chemical bath deposition process is another versatile synthesis strategy employed in the literature for achieving the uniform deposition of metal species on TiO$_2$, as reported by Chang et al., for the fabrication of Cu$_2$O on mesoporous TiO$_2$ beads (MTBs), which facilitated the essential charge separation for an improved hydrogen generation rate (223 mmol h^{-1} g^{-1}).[9]
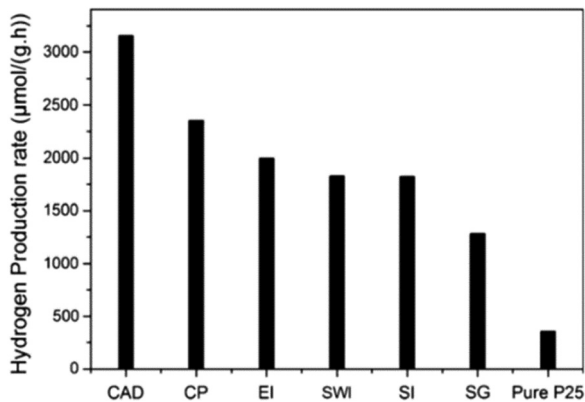
Fig. 17 Comparison of the photocatalytic hydrogen evolution rate on pure P25 and CuO/TiO₂ samples produced by different preparation methods, namely chemical adsorption decomposition (CAD), composite precipitation (CP), ethanol impregnation (EI), simple wet impregnation (SWI), stepwise impregnation (SI), and sol–gel (SG). Reproduced with permission from ref. 184. Copyright ©2014, Springer.

The synthesis strategy leading to the formation of TiO₂ with a sufficient amount of Ti⁴⁺ ions in tetrahedral coordination enhances the photocatalytic H₂ production rate due to fact that the photocatalytic activity of TiO₂-based catalysts depends on the quantity of Ti⁴⁺ ions present in a tetrahedral environment.[185] Kumari et al. reported an impregnation method for the fabrication of functionalized carbon nanotubes (FCNTs) integrated with TiO₂ nanotubes (TiNTs), which showed a high performance (7476 μmol h⁻¹ g⁻¹) for the photocatalytic hydrogen evolution reaction due to the strong interaction between FCNTs and TiNTs and the well-dispersed nature of the catalyst.[67]

Careful control of the synthesis parameters and process variation are essential given that even a slight variation in the synthesis process may introduce a variety of defects and impurities that could improve or worsen the photocatalytic activity and stability of materials. Generally, anatase-phase TiO₂ exhibits higher activity than the rutile phase, but synthesis frequently results in mixed-phase materials, making property optimisation more challenging.

4.2. Effect of surface area

Surface area is a crucial factor that influences the photocatalytic performance of a catalyst. Given that photocatalytic hydrogen generation is a surface-based phenomenon, a catalyst with a high specific surface area can offer more adsorption sites and photocatalytic reaction centers.[45] Khore et al. performed a comparative study of the photocatalytic performance of pristine TiO₂ and Au@TiO₂ photocatalysts for hydrogen generation under natural sunlight and arrived a correlation between their surface area and activity.[166] As illustrated in Fig. 19, among the studied catalysts, 2 wt% Au-loaded TiO₂ with the highest surface area (60 m² g⁻¹) showed the highest activity with an H₂ yield of 3.99 mmol g⁻¹ h⁻¹, and the activity decreased as the surface area decreased.[166]

In another variation, among different TiO₂-NT (nanotube)-based photocatalysts (TiO₂-NT, TiO₂-NT/ZnO-NR (nanorod), TiO₂-NT/ZnO-NR/Ag-NP (nanoparticle), TiO₂-NT(nanotube)/Pd-NDs (nanodendrites)) employed for photocatalytic H₂ production under one sun conditions using an H₂O/MeOH (1:2) mixture, the TiO₂-NT(nanotube)/Pd-ND catalyst having the highest surface area showed the highest hydrogen generation rate of 143.1 μmol h⁻¹.[173] Mishra et al. synthesized 15 wt%
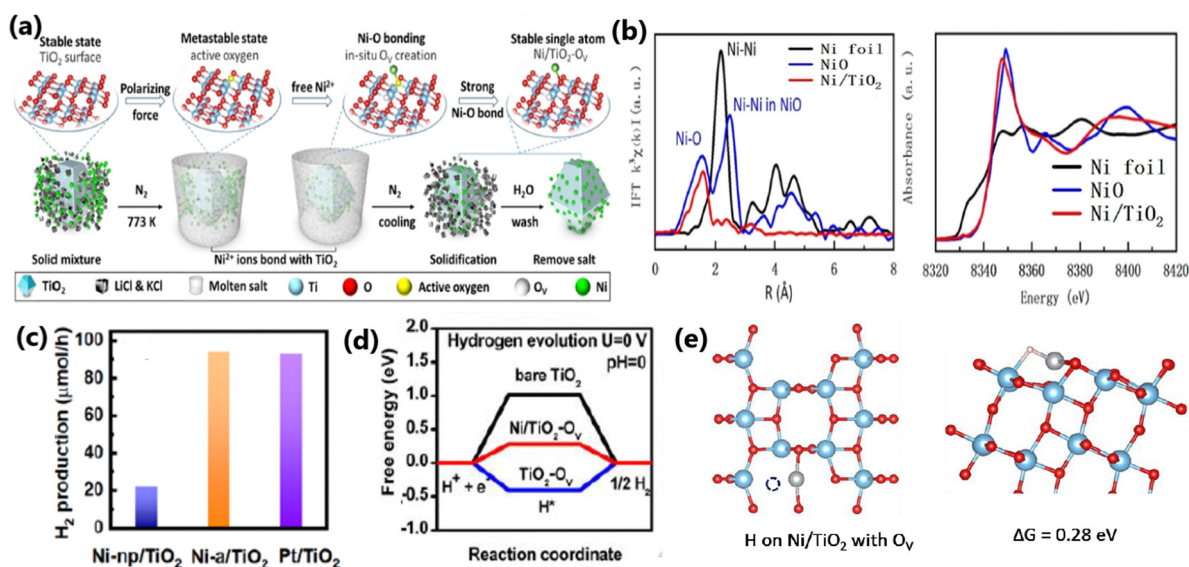

Fig. 18 (a) Schematic illustration of molten salt-mediated preparation of atomic Ni on TiO₂. For the TiO₂ molecular structure, (b) EXAFS and XANES spectra of Ni/TiO₂, respectively. Ni loading amount: 0.46 wt% (c) Comparison of H₂ evolution activity on Ni-np/TiO₂, Ni-a/TiO₂ and Pt/TiO₂ with the same loading amount (∼0.5 wt%). Experimental condition: 50 mg of sample dispersed in 100 mL of 10 vol% methanol aqueous solution (278 K) under an irradiation of a 300 W Xe lamp. (d) Free energy versus the reaction coordinates of different active sites. The simulation is based on the (101) facet of anatase TiO₂. (e) Molecular models of Oᵥ on Ni/TiO₂ and the corresponding formation energy of Oᵥ. Reproduced with permission from ref. 172. Copyright© 2020, Wiley-VCH.
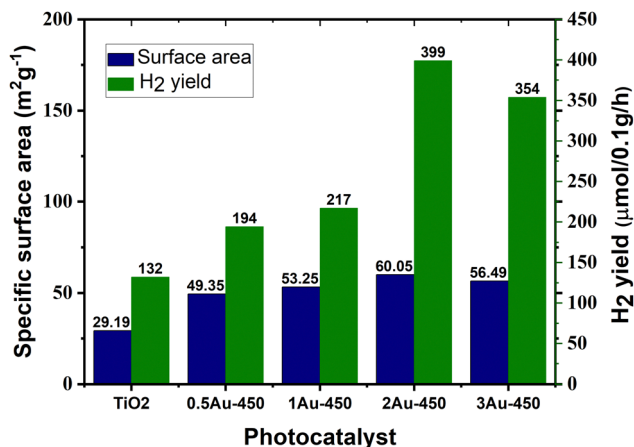
Fig. 19 Amount of hydrogen produced *vs.* surface area of photocatalyst for Au@TiO$_2$:0.5Au-450, 1Au-450, 2Au-450 and 3A-450 under natural solar light. Adopted from ref. 166. Copyright ©2018, the Royal Society of Chemistry.

S-modified TiO$_2$/β-SiC and showed that the high photocatalytic hydrogen evolution activity of the catalyst is due to its high specific surface area.[45]

A 2D TiO$_2$/g-C$_3$N$_4$ photocatalyst with 20 wt% TiO$_2$ having a high specific surface area showed a 2.4-times higher photocatalytic hydrogen evolution rate than g-C$_3$N$_4$ nanosheets having a relatively low specific surface area. The high photocatalytic activity of 2D TiO$_2$/g-C$_3$N$_4$ is due to its high surface area, and hence higher number of available active sites for hydrogen production.[181] Another way of utilizing the advantage of the high surface area in improving the photocatalytic H$_2$ production rate of titania is by modifying it in the form of silica-embedded titania and/or titania silica mixed oxide.[87] Although the correlation between surface area and photocatalytic activity has been demonstrated in the literature, there are some reports showing that surface area hardly had any influence on the photocatalytic activity and H$_2$ production rate in comparison with other favourable factors, as illustrated in the case of CuO/TiO$_2$ heterojunction and Pt@CuO/TiO$_2$ composites synthesized employing TiO$_2$ nanosheets and nanorod precursors.[186] Further, a high surface area is invariably associated with high porosity (with micro and mesopores) and large number of surface defects and can act as recombination centers. Considering these contradicting views, caution should be exercised when deriving a proper conclusion and proceeding further in photocatalysis.

4.3. Effect of calcination temperature

In majority of cases, the photocatalytic performance of a catalyst and its hydrogen production rate may be influenced by its calcination temperature. The calcination temperature may affect the crystallinity,[131] particle size,[187] phase characteristics,[131] oxidation state of the dopant,[182] porosity,[100] surface area,[43] number of active sites,[188] and morphology[189] of the photocatalyst. In general, an active photo-catalyst material shows relatively low activity at a low calcination temperature due to its poor crystallinity, and thus an optimum calcination temperature is required to achieve the desired physico-chemical characteristics for the

maximum photocatalytic performance.[131] The TiO$_2$ photocatalyst crystallized in the pure anatase phase undergoes an anatase-to-rutile phase transformation starting from a calcination temperature of around 500 °C to 800 °C. However, it is worth noting that the calcination temperature can vary depending on the specific phase requirements of TiO$_2$.

In general, the photocatalytic activity of TiO$_2$ is mainly contributed by the anatase phase due to its high surface area and small particle size; however, as the calcination temperature increases, the content of the less photocatalytically active rutile phase increases.[190] Thus, TiO$_2$-based photocatalytic materials show the maximum hydrogen generation at a calcination temperature range of 300–500 °C.[190] Besides, as the calcination temperature increases, the probability of charge carrier recombination at the bulk traps also increases.[53] The contribution of the anatase phase to enhancing the photocatalytic H$_2$ evolution reaction rate has been exemplified in the literature.[191] Among the different N-doped TiO$_2$ samples prepared at different calcination temperatures ranging from 300 °C to 800 °C, NTP-400 (N-doped TiO$_2$ calcined at 400 °C) showed the highest rate of photocatalytic hydrogen production due to the formation of highly crystallized anatase phase and incorporation of N in the crystal lattice.[189]

Sun *et al.* reported that the calcination temperature affects the photocatalytic hydrogen evolution activity of TiO$_2$-based photocatalysts because the anatase-to-rutile ratio in TiO$_2$ varies with the calcination temperature.[191] Camposeco *et al.* prepared 0.5Rh/TSG(TiO$_2$) *via* the sol–gel method and studied its photocatalytic performance as a function of calcination temperature (100 °C, 200 °C, 300 °C, 400 °C and 500 °C) for the water splitting reaction using 50% (v/v) ethanol–water mixture under a UV Pen-Ray Hg lamp (λ = 365 nm). As illustrated in Fig. 20a, 0.5Rh/TSG prepared at 400 °C (anatase) showed the highest H$_2$ production rate of 7246 μmol h^{-1} g^{-1}.[51]

A comparison of the photocatalytic H$_2$ evolution activity of Ru (wt% = 8.0)/TiO$_2$NB (nanobelts) non-annealed sample and the same catalyst calcined at different temperatures (200 °C, 400 °C, 600 °C, and 800 °C), as illustrated in Fig. 20b, revealed that Ru 8.0/TiO$_2$ NBs calcined at 400 °C showed the highest photocatalytic hydrogen production rate of 25.34 mmol h^{-1} g^{-1}.[47] The improved activity of Ru 8.0/TiO$_2$ NBs@400 °C is due to its improved crystallinity with the formation of the crystalline-phase Ru/RuO$_2$ and formation of an intimate junction between Ru/RuO$_2$ and TiO$_2$. With a further increase in the calcination temperature, an increased amount of RuO$_2$ was formed due to the oxidation of Ru, which had a detrimental effect on the rate of hydrogen evolution.[47]

The majority of researchers tried to maintain a greater anatase phase content in TiO$_2$. This is because although the rutile phase is stable, it has poorer photocatalytic activity compared to anatase because of its larger bandgap and smaller surface area. Thus, if this phase transition is not properly managed, the photocatalytic efficiency may significantly decline. Furthermore, high calcination temperatures can lead to particle growth and agglomeration, which reduces the surface area and active sites for photocatalytic reactions. Alternatively, inadequate calcination may result in the presence of
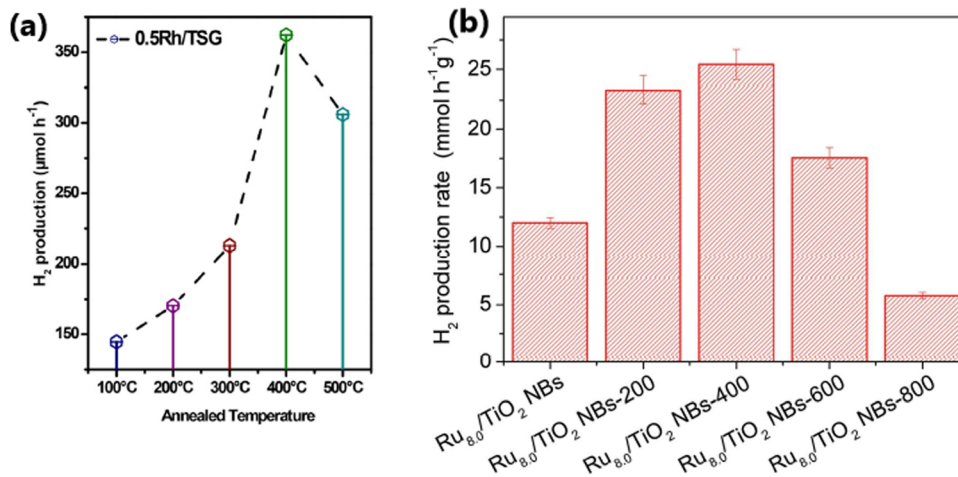
Fig. 20   (a) Variation in the rate of hydrogen production on 50 mg of 0.5Rh/TSG(TiO$_2$) as a function of calcination temperature (reproduced with permission from ref. 51. Copyright ©2018 Elsevier Ltd). (b) Variation in the rate of hydrogen production as a function of calcination temperature for the Ru (wt% = 8.0)/TiO$_2$ NB photocatalyst (reproduced with permission from ref. 47. Copyright ©2016, Wiley-VCH).

leftover organic matter or partially degraded precursors, which can serve as recombination sites for charge carriers produced during the photocatalytic process and hinder the activity.

4.4. Effect of morphology

The morphology of TiO$_2$ plays a considerable role in deciding the photocatalytic hydrogen evolution activity by affecting the interaction between the dopant and TiO$_2$,[186] migration of photogenerated electrons,[179] and effectiveness of the heterojunction.[179,186] TiO$_2$-based photocatalysts with specific morphologies such as nanosheets,[186] nanorods,[186] and nanotetrahedrons[167] have been studied for understanding the influence of morphology on photocatalytic H$_2$ production. The TiO$_2$ nanosheet with single-crystal structure and low density of defects was found to be highly effective in reducing the charge carrier recombination, thereby enhancing the rate of hydrogen evolution.[186]

Wang *et al.* fabricated a 2D/1D heterojunction of TiO$_2$/CdS composite with (001) facets of TiO$_2$ and CdS nanorods, which showed a photocatalytic hydrogen evolution rate of 128.3 mmol g^{-1} h^{-1} with acetic acid-water mixture (20 mL acetic acid in 210 mL water) under visible light (300 W Xe arc lamp; $\lambda > 400$ nm), which is much higher than that by the conventionally prepared P25/CdS (35.3 mmol g^{-1} h^{-1}).[179] The outstanding photocatalytic performance of 2D/1D TiO$_2$/CdS is attributed to the morphological features of TiO$_2$ and the formation of an optimized 2D/1D heterojunction, leading to efficient charge separation and enhanced electron transport. The morphology of the cocatalyst also plays a vital role in enhancing the photocatalytic H$_2$ production rate. Thus, between TiO$_2$–Pd NSs (nanosheets) and TiO$_2$–Pd NTs (nanotetrahedrons), the photocatalytic hydrogen production rate was higher on TiO$_2$ integrated with ultrathin nanosheets of Pd due to the rapid generation of hot electrons and their transfer from Pd nanosheets.[167] A comparison of the morphological features, optical properties and photocatalytic activities of TiO$_2$–Pd nanosheets and TiO$_2$–Pd nanotetrahedrons is shown in Fig. 21.

The photocatalytic H$_2$ production activity of the Pt@CuO/TiO$_2$ composite fabricated using TiO$_2$ nanosheets was higher than that of Pt@CuO/TiO$_2$ prepared using TiO$_2$ nanorods.[186] The relatively high activity of the nanosheet-based photocatalyst is due to a variety of reasons, as follows: (1) TiO$_2$ nanosheets mainly have exposed relatively high surface energy (001) facets, whereas TiO$_2$ nanorods are dominated by comparatively lower surface energy (101) facets, (2) CuO has stronger interactions with TiO$_2$ nanosheets than with TiO$_2$ nanorods, (3) CuO can form a more stable p–n heterojunction with TiO$_2$ nanosheets, and (4) TiO$_2$ nanosheets have a low density of defects, which reduce the possibility of charge recombination. Compared to conventional Pd/P25 TiO$_2$, Pd/TiO$_2$ nanosheets showed relatively higher activity for photocatalytic H$_2$ production due to the greater number of exposed high surface energy (001) facets on nanosheets.[170] In contrast, for the nanorod morphology, the aspect ratio is crucial for enhancing the photocatalytic water splitting, as reported by Fu et al. for nanorods of rutile TiO$_2$.[192] The different works discussed above show that due to the larger surface area and more active sites, nanostructured TiO$_2$ materials such as nanotubes, nanorods, and nanospheres generally show improved photocatalytic activity compared to bulk materials. Nevertheless, the production of these nanostructures frequently necessitates precise control of the synthesis parameters and more sophisticated and expensive techniques.

4.5. Crystallographic facet-dependent activity

Certain exposed facets of TiO$_2$ can enhance the solar hydrogen generation to a large extent because of the effective electron–hole separation by way of enhancing the interfacial charge transfer, more exposed surface area, and high surface energy.[136,170] The choice of TiO$_2$ with unique tailored facets {001} or {101} in the composite has a significant influence on the photocatalytic hydrogen evolution performance.[136,170,192,193] Liu *et al.* studied the influence of the (100), (001), and (101) crystal facets of TiO$_2$ on the photocatalytic hydrogen generation activity of a TiO$_2$–
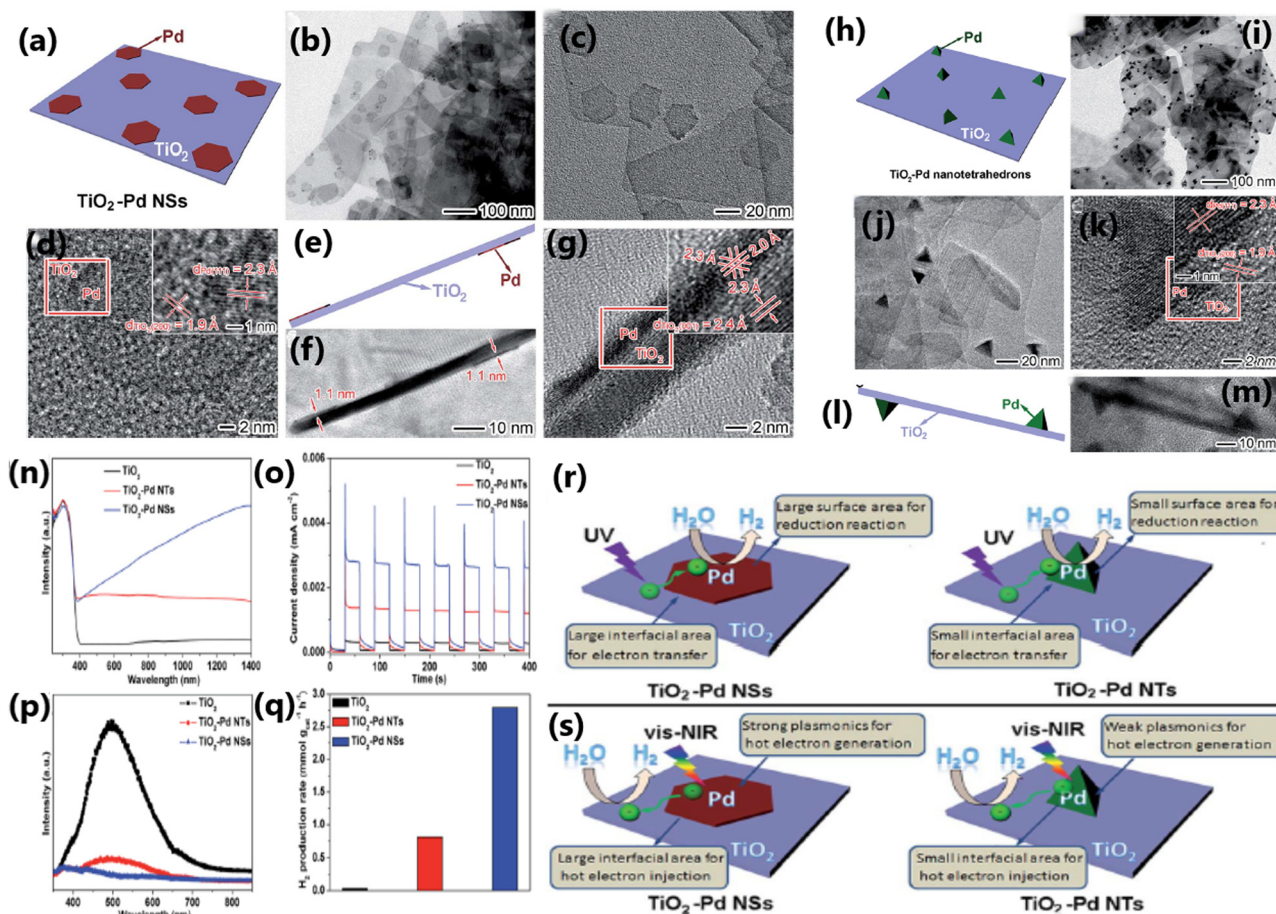
Fig. 21 (a) Schematic illustration, TEM (b and c), and HRTEM (d) images of TiO_2−PdNSs. (e) Schematic diagram, TEM (f), and HRTEM (g) images of TiO_2−Pd NSs with TiO_2 nanosheets. (h) Schematic illustration, TEM (i) and (j), and HRTEM (k) images of TiO_2−Pd NTs. (l) Schematic illustration and TEM (m) image of TiO_2−Pd NTs with TiO_2 nanosheets. UV-vis diffuse reflectance spectra (n), photocurrent response (o), PL spectra (p) and photocatalytic H_2 production performance (q) of bare TiO_2, TiO_2−Pd NTs and TiO_2−Pd NSs. Schematic illustrating the photocatalytic H_2 evolution reaction on the samples of TiO_2−Pd NSs and TiO_2−Pd NTs (r) under UV and (s) vis-NIR light irradiation, respectively. Reproduced with permission from ref. 167. Copyright ©2016, the Royal Society of Chemistry.

graphene composite and observed that the TiO_2-100-graphene composite exhibited the highest rate of hydrogen evolution.[152] The enhanced activity of the Ti-100-G composite was attributed to the formation of Ti–C bonds, which increased the rate of charge transfer, and thereby improved hydrogen production activity. In contrast, Ti–O–C bonds are formed in the Ti-001-G and Ti-101-G composites, leading to a reduced charge transfer rate and lower hydrogen evolution activity. Due to its very poor interfacial connections and unfavourable electronic structure, the Ti-001-G composite showed the lowest rate of hydrogen evolution.[152] The preparation of TiO_2–graphene nanocomposites, their physicochemical characteristics and a schematic illustration of the atomic structures of the interfaces between graphene and different TiO_2 crystal facets and their photocatalytic process, and the photocatalytic H_2 production activities are provided in Fig. 22.

Exposed facets of certain dopants can also influence the rate of hydrogen generation due to the formation of appropriate energy levels and reduced rate of electron–hole recombination by trapping the photogenerated electrons. For example, The Pt/

TiO_2 photocatalyst having (111) facets of Pt with a higher Fermi level is highly effective for trapping the electron in the conduction band of TiO_2 than that with the (100) facets of Pt.[188] In another study, Qi et al. reported that a CdS-sensitized Pt/TiO_2 nanosheet photocatalyst with (001) exposed facets showed outstanding water splitting activity due to the special electronic and surface properties of the (001) facets.[194] Compared to {101}-TiO_2/CdSe QDs, the relatively high photocatalytic production rate shown by {001}-TiO_2/CdSe QDs is due to the enhanced charge separation and efficient electron transfer from CdSe QDs to the (001) facets of TiO_2.[136] Due to the differences in their surface energy, reactive site density, and charge carrier dynamics, different facets of TiO_2 exhibit different photocatalytic activities. Hence, facet-controlled synthesis methods are required to maximise the photocatalytic performance. For example, nanocube and octahedron morphologies only expose (100) or (111) facets, respectively, while truncated octahedron exposes both (100) and (111) facets. Thus, by fine tuning these methods, it is possible to improve the performance of photocatalysts and well-defined synthetic methodologies are required.
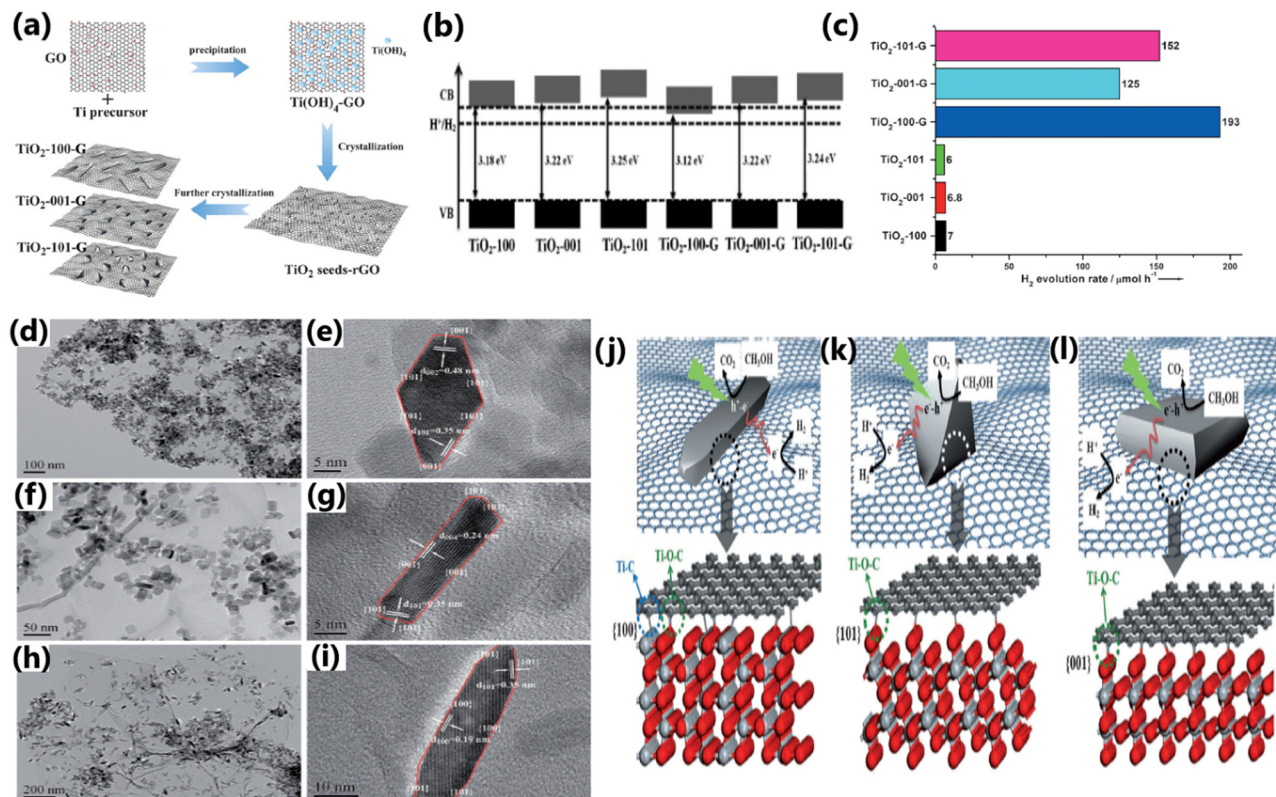
Fig. 22 (a) Schematic illustration of the preparation of TiO$_2$–graphene nanocomposites with controllable TiO$_2$ crystal facets exposed. (b) Band structures of TiO$_2$ and TiO$_2$–graphene nanocomposites. (c) H$_2$ evolution rates from methanol solution catalyzed by TiO$_2$ and TiO$_2$–graphene nanocomposites. (d)–(i) TEM and HRTEM images: (d) and (e) TiO$_2$-101-G, (f) and (g) TiO$_2$-001-G, and (h) and (i) TiO$_2$-100-G. Schematic illustration of atomic structures of interfaces between graphene and different TiO$_2$ crystal facets and the photocatalytic process by TiO$_2$–graphene nanocomposites: (j) TiO$_2$-100-G, (k) TiO$_2$-101-G, and (l) TiO$_2$-001-G. Reproduced with permission from ref. 152. Copyright ©2014, Wiley-VCH.

4.6. Particle size

Particle size can significantly affect the performance of photocatalysts by affecting the number of active sites, charge transfer and electron–hole recombination rates, and light penetration.[136,137] Photocatalysts with a smaller particle size possess a large number of active sites and accelerated electron transfer process.[117] Contrarily, large-sized catalyst particles not only reduce the number of active interfaces but also block the penetration of incident light.[118] Also, the particle size of metal dopants influences the energy separation between the Fermi level of the metal and the conduction band of TiO$_2$, which directly affect the carrier separation ability of the photocatalyst.[195] In the case of SPR metals such as Ag and Au, their absorption wavelength varies with their particle size and morphology.[39,196] Dopants with small-sized particles facilitate a high dispersion of particles on crystalline TiO$_2$. However, metallic particles with a very small size show poor stability due to the high surface energy and easy detachment of particles from the TiO$_2$ surface when stirred intensely.[197] This suggests that material integration is of great significance for any sustainable operation for long reaction time.[198] Yang et al. reported that for a given gold loading, Au@TNT with a reduced particle size showed an improved photocatalytic performance and attributed to the high dispersion of Au particles on the surface of TiO$_2$ and its modified electronic properties.[168] Metal nanoparticles with a small particle size produce an increased amount of highly energetic surface sites,

which make the catalyst highly effective for photo-injection and enhance the electron transfer process. The modified electronic state has a positive effect by improving the charge transfer and electron–hole separation efficiency.[168] The superior photocatalytic H$_2$ production activity due to highly dispersed Cu^0 nanoparticles in Cu–TiO$_2$ MS (mesoporous microporous) photocatalyst,[197] small-sized Au nanoparticles in Au-loaded mesoporous S,N-TiO$_2$ (SNT),[199] and Pd and Pt nanoparticles in TiO$_2$[195] substantiate the importance of controlling the metal particle size to achieve the desired properties and enhancing the photocatalytic efficiency.

Metal nanoparticles such as Au and Pt with a size in the range of 1–10 nm supported on TiO$_2$ lead to an increase of energy gap between the Fermi level of metal nanoparticles and the conduction band of TiO$_2$, resulting in improved charge separation and enhanced hydrogen production activity.[195] Gold nanoparticles were synthesized via a seed-mediated growth method for the sensitization of Pt/TiO$_2$ catalysts (Fig. 23a) and it was evident from the TEM images (Fig. 23b–e) that narrow-sized Au particles were obtained through this method. Among the Au-sensitized Pt/TiO$_2$ photocatalysts with different particle sizes of Au (10, 20, 30, and 50 nm) for photocatalytic hydrogen production, the Au nanoparticles with a particle size of 20 nm showed the highest performance under visible light (Fig. 23g and h).[200] The size of Au nanoparticles is clearly evident from the TEM images, as illustrated in Fig. 23, and
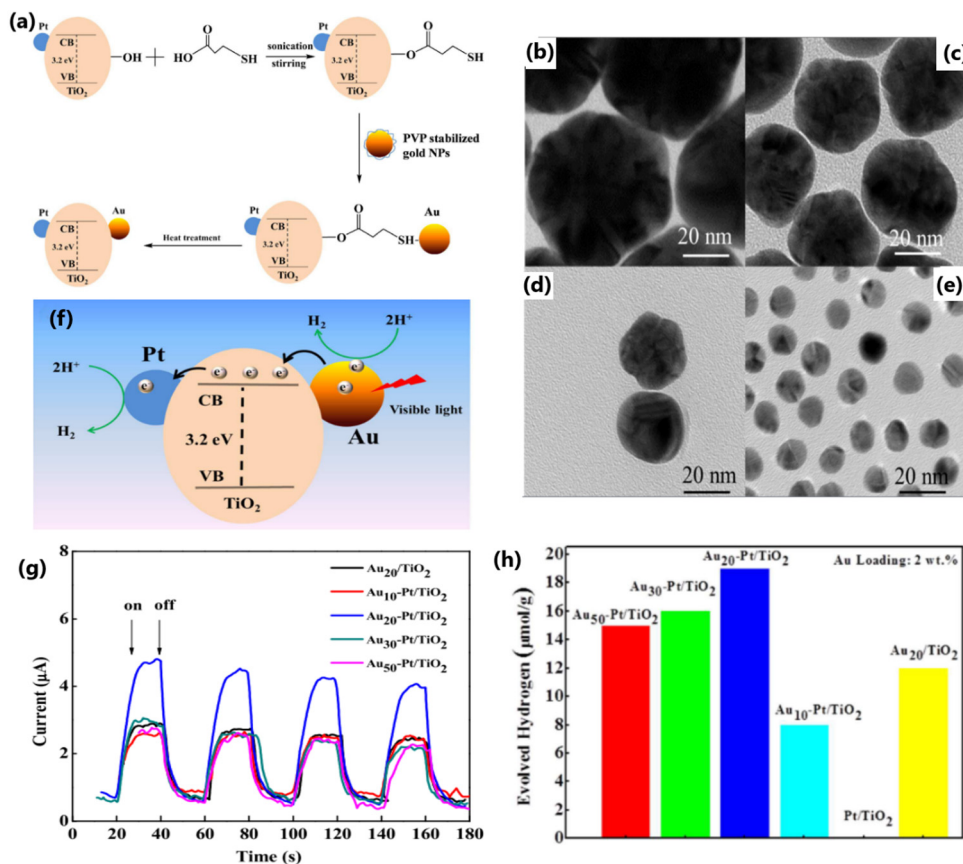
Fig. 23 (a) Schematic diagram of the synthesis of Au nanoparticles supported on Pt/TiO$_2$ composite catalysts. TEM images of the synthesized gold nanoparticles with a size of approximately 50 nm (b), 30 nm (c), 20 nm (d), and 10 nm (e). TEM images of Pt/TiO$_2$. (f) Plausible photocatalytic mechanism of Au-sensitized Pt/TiO$_2$ under visible light. (g) Photocurrent response of Au nanoparticles with different sizes supported on Pt/TiO$_2$ nanocomposites under visible-light irradiation ($\lambda > 420$ nm). (h) Hydrogen-production activity of different catalysts under visible-light irradiation ($\lambda > 420$ nm) in water/methanol mixture. Reproduced with permission from ref. 200. Copyright ©2017, the American Chemical Society.

the results show that the SPR effect and the electron injection into the CB of TiO$_2$ depends on the particle size of Au (Fig. 23f and h).[200] Generally, smaller particles possess a large surface area and a greater number of reaction sites per unit weight of catalyst. Nonetheless, smaller particles can sometimes lead to a decline in photocatalytic activity with time due to particle aggregation. If the size of the particles is smaller than twice the width of the space charge layer, the extent of band bending decreases, which eventually diminishes the potential to separate e$^-$/h$^+$ pairs. Alternatively, visible light-absorbing small quantum dots could be grown inside the pores of a wide bandgap semiconductor and this approach is likely to result in higher activity due to the inherent and inevitable formation of heterojunctions.

4.7. Porosity

The porosity of a photocatalyst has a significant influence on its photocatalytic hydrogen production rate given that it increases the surface area, providing a large number of exposed surface sites, enhances the absorption of a large number of reactant species, enhancing the light absorption performance, and increases the mass transfer rate.[15,88,201] A macroporous channel in a photocatalyst can increase the mass transfer within the

macro-mesoporous framework and enhance the light absorption performance.[15] The presence of a meso-macroporous network in a TiO$_2$ photocatalyst improved its light-harvesting ability by transferring the incident photon flux into the internal surface of mesoporous TiO$_2$ through multiple internal reflections.[155] This type of macro-mesoporous architecture additionally supports the easy channelization of photogenerated electrons via the mesoporous walls and facilitates the electron transportation to the surface of TiO$_2$ via the microporous channel. Consequently, the electron–hole recombination is suppressed and the photocatalytic activity is enhanced.[182] The 3D ordered macroporous Pt/TiO$_2$–ZrO$_2$ composite synthesized using a combination of vacuum impregnation and photoreduction method, for example, exhibited high photocatalytic water splitting activity to H$_2$ due to the enhanced light absorption effected through multiple internal reflections in its pores.[155]

A comparison of the H$_2$ evolution activity between Pt-deposited mesoporous TiO$_2$ nonporous Pt/TiO$_2$-P25 revealed that mesoporous Pt/TiO$_2$-450 showed better activity than nonporous Pt/TiO$_2$-P25 because the mesoporous network facilitates efficient charge transfer by forming suitable interfaces and the reactants can easily diffuse through the pores.[202] Li *et al.*

reported that the CuO/TiO_2 photocatalyst prepared by the chemical adsorption decomposition method (CAD) consisted of a large number of small pores, which facilitated the absorption of a large number of reacting molecules on its surface due to the presence of more active sites and promoted the hydrogen generation activity.[184] One of the reasons for the enhanced H_2 production rate displayed by the Au-deposited mesoporous S,N-TiO_2 (SNT) photocatalyst with a pore diameter in the range of 8 to 13 nm is due to its mesoporous nature, which enhanced the light-harvesting ability of the material.[199] Further, using green leaves and highly porous architecture was proved to be beneficial for photocatalysis and light harvesting applications.[203,204] For example, Devaraji *et al.* demonstrated the use of a green leaf as a template to produce an inorganic leaf to produce ZnO with a nano-micro architecture and demonstrated its use for the efficient oxidation of benzene to phenol under UV light. In another work, Chen and coworkers demonstrated the importance of the porous architecture for enhanced photocatalytic H_2 production by fabricating TiO_2 nanotube arrays (TNTAs) grown on titanium fiber of a titanium web (TNTA-web) and titanium foil (TNTA-foil).[205] The TNTA-web generated 40 mmol h^{-1} m^{-2} of hydrogen, while the TNTA-foil failed to produce hydrogen under similar conditions. Further, the addition of the same amount of Pd nanoparticles to the TNTA-web and TNTA-foil resulted in an increase in the production rate to 130 and 10 mmol h^{-1} m^2, respectively. The enhanced photocatalytic H_2 production activity of the TNTA-web material was attributed to its unique dual porosity. The synthesis procedure and morphological analysis of TNTA-web are depicted in Fig. 24. Photocatalysts having dual porosity, such as hierarchical porous-structured materials containing a combination of macroporosity and mesoporosity, are believed to be more advantageous than single porosity. However, more research in this direction is needed for proper control of the porosity, which can be achieved by careful variation of the synthesis parameters and/or adopting novel synthesis strategies. Establishing a structure–activity relation is an interesting aspect in photocatalytic research, which deserves more attention.

4.8. Amount of catalyst

The rate of photocatalytic hydrogen evolution also relies on the quantity of catalyst to a large extent. In general, the catalyst shows the maximum photocatalytic performance at an optimal amount, and with an increase in the amount of catalyst, the photocatalytic H_2 evolution, generally decreases and/or levels off, which can be explained by the following reasons:[182] (1) at higher concentrations of photocatalyst, there is a reduction in the light penetration depth in the suspension of catalyst; further, light scattering occurs more in a suspension compared to light absorption. (2) An excess amount of catalyst may increase the electron–hole recombination rate. (3) The aggregation of catalyst particles is generally high in slurry form with an uneven distribution of particles, resulting in a vast differences in contact and reaction rate, and hence the diffusion of reactants and photogenerated charges towards the reaction sites is less effective in the suspension form. (4) The active site of the catalyst can be covered up by the presence of a large quantity of catalyst.[43]

The photocatalytic performance of Ag/TiO_2 in water splitting reaction for different catalyst amounts revealed that the H_2 production rate increased initially with an increase in the catalyst concentration from 15 to 20 mg L^{-1}, and with a further increase in catalyst concentration, the activity declined (see Fig. 25a).[112] The catalyst in excess amount may hinder the absorption of radiation, and in certain cases it accelerates the electron–hole recombination.[112] The amount of catalyst needed for achieving the optimum activity may vary as the nature of the catalyst, catalyst composition and reaction conditions vary.
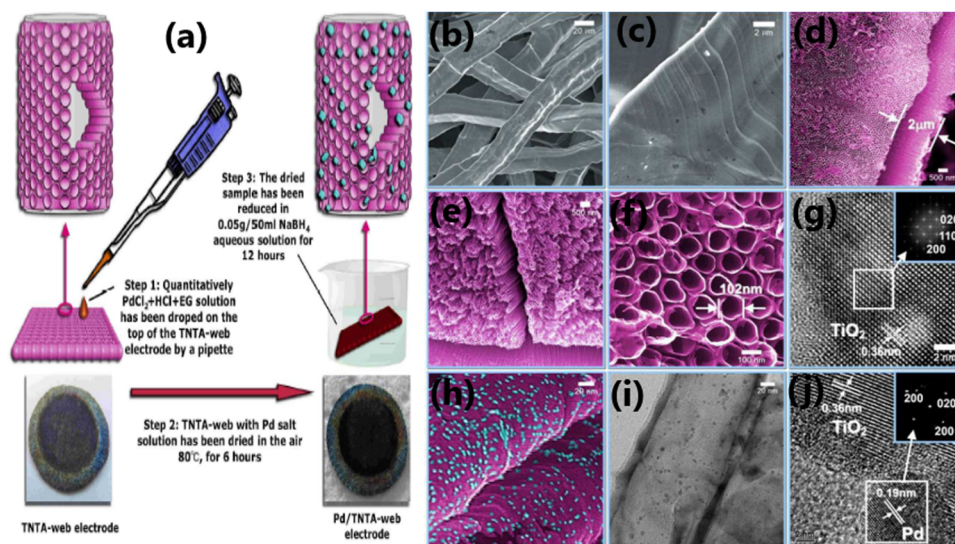

Fig. 24 (a) Synthesis of Pd/TNTA-web (3D TiO_2 nanotube array). Scanning electron microscopy (SEM) images of the pristine titanium-web substrate (b) and (c) and TiO_2 nanotubes arrays on the web (d), (e) and (f). HR-TEM image of a nanotube (g), SEM image (h), TEM image (i) and HRTEM image (j) of the TNTA-web with 0.1 mg cm^{-2} Pd (0.26 wt%). Reproduced with permission from ref. 205. Copyright ©2018, the Royal Society of Chemistry.

For example, as illustrated in Fig. 25b, the H$_2$ production rate on Ni/γ-Al$_2$O$_3$/CNT-TiO$_2$ was the maximum with 10 mg catalyst and the activity decreased with a further increase in catalyst amount.[102] The excess amount of catalyst adversely affected the light penetration, which decreased the overall catalytic performance.[102] In fact, an earlier review[66] listed the very high activity associated with a small amount of catalyst (1–3 mg in ∼50–100 mL solution), whereas a larger quantity of the same catalysts (10–200 mg in ∼50–200 mL solution) showed a large drop in hydrogen production activity. The large difference in activity is attributed to the significant light scattering with a larger amount of catalyst quantity, whereas efficient light absorption with a small quantity of catalyst in large volumes of solution. Based on the available literature and above discussion, it can be concluded that careful optimisation of the amount of photocatalyst is necessary to extract the best catalytic performance from a photocatalytic material. Nonetheless, how it can be scaled-up for large volume applications also needs to be addressed. Although this is an engineering issue, this thinking is likely to bring clarity and minimize the problems in the future.

4.9. Amount of dopant

The photocatalytic activity of TiO$_2$ can be drastically improved by using various dopants. However, the amount of dopant is a critical factor in photocatalysis. It has been observed that TiO$_2$-based composites for a given dopant show the maximum performance at an optimum concentration in the TiO$_2$ matrix, and with a further increase in the dopant concentration, the photocatalytic activity decreases.[85] A high concentration of dopant in TiO$_2$ acts as the recombination center for electrons and holes[85] and block the surface active sites. This reduces the light utilization ability of the catalyst and reaction rate, and thereby the photocatalytic hydrogen production rate decreases.[134] An increase in the loading of dopants may also cause the agglomeration of particles and particle growth rather than their uniform distribution.[104] However, an optimum amount of dopant can effectively separate the electrons and holes and enhance the charge transfer through the interface between TiO$_2$ and the dopant and its efficient utilization

during the photocatalytic reaction. There are several reports available in the literature illustrating the effect of dopant concentration on the photocatalytic H$_2$ production activity.

As illustrated in Fig. 26a, the photocatalytic H$_2$ evolution activity of Cu-decorated TiO$_2$ containing different wt% of Cu (1, 2, 3, 4, and 5 wt%) revealed that the amount of hydrogen produced increases up to 3 wt% of Cu (3.33 mmol g^{-1} h^{-1}), and with a further increase in Cu concentration, the activity is reduced.[104] This study revealed that 3 wt% Cu is the optimum concentration to achieve the maximum activity, and at a higher concentration of Cu (above 3 wt%), the aggregation of Cu particles occurs on the surface of TiO$_2$ and these agglomerated Cu nanoparticles act as recombination centers for photogenerated electrons and holes. This shows that a suitable mass ratio of components is crucial to generate an efficient interface for excellent photocatalytic hydrogen evolution.

In another variation, the photocatalytic hydrogen production activity of Cu$_2$O–TiO$_2$/rGO revealed that TiO$_2$ with the optimum Cu loading of 1 wt% and GO loading of 3 wt% showed the maximum performance because of the enhanced charge transfer and excellent light absorption capacity of the material. The highest photocatalytic H$_2$ production activity was observed with 3 wt% Au-loaded mesoporous S,N-TiO$_2$ when Au-deposited mesoporous S,N-TiO$_2$ with different wt% of Au (0.5, 1, 2, 3, 4 and 5) were compared for the reaction.[199] In this case, a high content of gold blocked the active sites and obstructed the penetration of light into the catalyst surface. The high concentration of metal on the surface of TiO$_2$ may also act as electron–hole recombination centres, which reduces the rate of photocatalytic hydrogen production.[85] When a combination of metal nanoparticles is employed for the fabrication of TiO$_2$-based composites, the uniform distribution of all the metal nanoparticles on TiO$_2$ is crucial to achieve the maximum photocatalytic performance.[85]

Reddy et al. reported that a bimetallic Cu/Ag@TNT-2 (CAT-2) photocatalyst with the optimum amount of Ag and Cu prepared using a mixture of 0.1 M Cu and 0.1 M Ag precursor showed the highest rate of photocatalytic hydrogen generation due to the uniform dispersion of Ag and Cu on TiO$_2$.[99] A lower number of
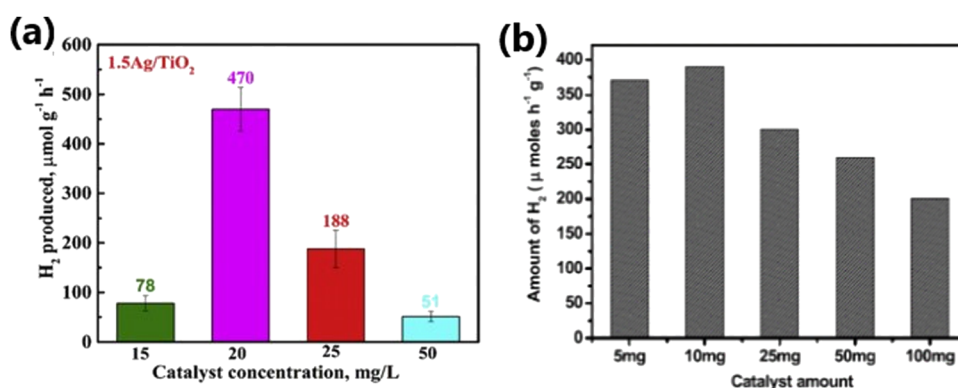

Fig. 25 (a) Photocatalytic hydrogen evolution activity of Ag/TiO$_2$ by varying the amount of catalyst. Reproduced with permission from ref. 112. Copyright ©2019, Elsevier Ltd. (b) Variation in photocatalytic H$_2$ evolution rate with respect to the amount of Ni/γ-Al$_2$O$_3$/CNT-TiO$_2$ catalyst. Reproduced with permission from ref. 102. Copyright ©2017, Elsevier Ltd.

active sites was present at a low concentration of Cu and Ag on the surface of TiO_2, whereas a high concentration of metal nanoparticles led to poor electron transfer.[99] Wei *et al.* reported that a TiO_2–Ni hybrid photocatalyst with the optimum Ni amount of 1 mol% showed the highest rate of hydrogen evolution during the photocatalytic water splitting reaction.[16] An excess Ni loading limited the light absorption ability and blocked the active sites of the catalyst, leading to a decrease in activity (see Fig. 26b).

The photocatalytic hydrogen evolution activity of Pd-integrated TiO_2 nanosheets revealed that the photocatalyst showed the highest activity with an optimum Pd loading of $0.1~\mathrm{mg~cm^{-2}}$.[205] The H_2 evolution activity decreased when the amount of Pd was higher than the optimum loading due to the increase in Pd particle size and incorporation of Pd atoms in the bulk part rather than on the surface of TiO_2. Moreover, the integration of a large amount of Pd in TiO_2 limits the expansion of the Pd–TiO_2 interface and reduces the number of charge carriers. The incorporation of a small amount of non-metal dopants such as N in anatase TiO_2 nanotubes creates defect centers, while maintaining the anatase phase, and strongly promotes the photocatalytic H_2 evolution performance of TiO_2 nanotube layers, whereas the high-dose N incorporation leads to amorphization of the incorporated region of TiO_2.[114] In conclusion, the effectiveness of TiO_2-based photocatalytic materials is highly sensitive to the amount of dopant used. Both insufficient and excessive dopant levels can significantly impair the photocatalytic efficiency by either failing to adequately enhance charge separation or by introducing recombination centres, respectively.

4.10. Thin film approach

Photocatalysts in thin-film form show a significantly higher performance than that in particulate form for hydrogen evolution.[165,206,207] The catalyst nanoparticles assembled in thin film are nearly uniformly spread across the substrate and have a large exposed surface area to the reactants and irradiation, resulting in more efficient interactions among the catalyst particles, light and reactants with relatively less mass transfer constraints. The possible reasons for the enhanced solar hydrogen evolution activity of photocatalysts fabricated in thin film form are as follows:[206] (1) by optimizing the film thickness to around 10 μm, the light absorption achieved is the maximum in thin films, while the same material in suspension form scatters light, rather than absorbing it; (2) the exposure of the maximum surface to solar radiation in thin film form is beneficial for enhancing the light-harvesting and light-induced electron excitation processes and increases the hydrogen production and apparent quantum yield (AQY); (3) the maximum utilization of surface area and active sites is possible in thin film form, which is good for the diffusion of charges toward the reaction sites; (4) better contact of catalyst nanoparticles is possible in the film form, which enhances the charge separation and charge utilization, whereas charge recombination is severe in powder form; and (5) thin film form with some surface roughness is beneficial for the internal scattering of light within the depth of thin films and enhances the charge carrier production/utilization. In powder form, additional energy in the form of electricity is needed for constant stirring to make the catalyst particles highly homogeneous in the reaction medium.[43,66,165,208] Unlike the case with solar cells, the charge carriers generated during the photocatalytic process are efficiently consumed within an ensemble of particles in a small area in thin film and hydrogen formation occurs from every part of the thin film. This indicates that the charge carriers do not need to diffuse long distances in the order of microns.[165,209]

A comparison of the solar H_2 production activity of titania (P25) and Pd/P25 fabricated in thin film form (4.69 cm^2) on a glass plate and their powder form counterparts revealed that the Pd/P25 catalyst (1 mg) fabricated in thin film form resulted in an H_2 production rate of $104~\mathrm{mmol~h^{-1}~g^{-1}}$, which was about 11–12-times higher than the Pd/P25 catalyst (25 mg) in powder form.[165] The digital photograph, FESEM images and photocatalytic performance of the prepared thin film are depicted in Fig. 27a–d. The enhanced activity of Pd/P25 in thin film form is

Fig. 26 (a) Variation in the H_2 evolution activity of TiO_2 decorated with different wt% of Cu. Reproduced with permission from ref. 104. Copyright ©2017, the Royal Society of Chemistry. (b) Rate of hydrogen evolution of TiO_2 and TiNi samples with different loadings of Ni. Reproduced with permission from ref. 16. Copyright© 2018, the Royal Society of Chemistry.

Fig. 27 (a) Digital photographs of thin films of P25 and Pd/P25. FESEM images of Pd/P25 thin films over a glass plate at a scale bar of 2 μm (b) and (c) cross-sectional view of a freshly cleaved thin film (scale bar: 10 μm). Inset in (c) shows the cracks. (d) Photocatalytic H_2 evolution activity in the particulate and thin film form of different catalysts (reproduced with permission from ref. 165. Copyright©2019, the Royal Society of Chemistry). (e) Photocatalytic H_2 production activity of mesoporous TiO_2 and Ag/TiO_2 nanocomposites, measured in thin-film form, in aqueous methanol solution under direct sunlight. Reproduced with permission from ref. 43. Copyright ©2021, Wiley-VCH.

due to its maximum exposed surface area to the reactants and sunlight and other advantageous aspects of thin film, as described above. A similar trend in the photocatalytic H_2 production activity of a catalyst in thin film form compared to its powder counterpart was also observed with Ag/TiO_2 nanocomposites (Fig. 27e).[43]

The excellent catalytic performance of Pd/TiO_2,[165] Ag/TiO_2,[43] $Cu-Ni/TiO_2$,[3] Cu_xO/TiO_2,[209] $Cu-Ag/TiO_2$[206] and $AuPd/C/TiO_2$[66] fabricated in thin-film form compared to their powder counterparts has been demonstrated in the literature. Tudu *et al.* reported that the thin film form of the $Cu-Ni/TiO_2$ (1:1 = Cu:Ni) photocatalyst exhibited an enhanced rate of hydrogen evolution (41.7 mmol h^{-1} g^{-1}) compared to its powder form (1.75 mmol h^{-1} g^{-1}) due to the efficient charge generation and its utilization in the film form, which mimicked the natural photosynthesis by green leaves.[3] In another report, the film form of the $AuPd/rGO/TiO_2$ photocatalyst displayed an enhanced hydrogen generation (21.5 mmol h^{-1} g^{-1}) performance compared to its powder form by a factor of 43 times. The higher activity of the film form of the catalyst is attributed to its high light absorption capacity, efficient contact between the particles, and remarkable charge generation and utilization.[66]

An important aspect of assembling and integrating thin films is to enhance the number of heterojunctions or Schottky junctions. A recent work on integrating $BiVO_4$ in the micro and mesopores of $P25-TiO_2$ showed a solar to fuel efficiency of 31% under one sun condition for artificial photosynthesis to produce methanol and formaldehyde. One of the main reasons attributed is the observation of 174 trillions of $BiVO_4-TiO_2$ heterojunctions in 1 mg of material, as reported by Salgaonkar *et al.*[210] To the best of our knowledge, this was the first time that the number of heterojunctions in a material was reported, which was calculated based on the pore-size distribution and

surface area by measuring them carefully before and after integrating $BiVO_4$ with TiO_2. This indeed opens a new window to fabricate highly integrated materials for efficient charge separation and their diffusion to the redox sites. Similar works may lead to an enhancement in light to chemical conversion for a variety of reactions.

5. Co-production of H_2 and value-added products (VAPs) from biomass components for the concurrent utilisation of electrons and holes

Despite the efficiency of utilizing sacrificial reagents as electron donors or hole scavengers to boost photocatalytic hydrogen production, their oxidized products are mostly ignored or unexplored. Recent studies indicated that some catalysts can produce oxidized products of sacrificial reagents together with H_2 due to the concurrent utilization of photogenerated electrons and holes.[211] Most of the studies usually use comparatively costlier sacrificial reagents such as methanol; however, if methanol can be converted to value-added products (VAPs) such as formic acid, the operating expenses of photocatalysis can be reduced. Moreover, the utilization of the biodiesel byproduct glycerol as a sacrificial reagent can lead to the coproduction of H_2 fuel together with VAPs. Compared to pure water-splitting systems, these coupled photocatalytic H_2 production systems will be more reactive and economical for H_2 generation. However, some challenges, such as the removal of liquid products from the reaction system, low conversion efficiency, and product

selectivity, need to be addressed. In this case, appropriate chemical process design, coupled with efficient separation techniques, can solve the former issue. Currently, the coproduction of H_2 and the generation of VAPs from sacrificial reagents are still in their infancy, and thus some advanced research in this field is required to tackle the obstacles and explore photocatalytic H_2 production coupled with the oxidation of sacrificial reagents with a wide range of sacrificial reagents, especially biomass-derived ones.[52]

A bifunctional p–n heterojunction of NiO–TiO$_2$ photocatalysts could simultaneously produce H_2 and VAPs such as glyceraldehyde and dihydroxyacetone from a glycerol–water solution (10% v/v) under UV-visible light irradiation.[211] The best-performing catalyst (7.5% Ni-loaded TiO$_2$) produced 8000 μmol h^{-1} g^{-1} hydrogen and could achieve 20% conversion of glycerol. Interestingly, at the beginning of the reaction, the yield of glyceraldehyde was higher than that of DHA; however, after 24 h of reaction, almost the same yields of both the products were obtained.

The reduction reaction occurs on the surface of TiO$_2$, while the glycerol oxidation occurs on NiO. The feasibility test revealed that glyceraldehyde contributes the highest share of annual earnings (89%), followed by dihydroxyacetone (11%) and H_2 (0.03%). The photocatalytic H_2 production performance, glycerol oxidation and corresponding reaction mechanism of NiO–TiO$_2$ photocatalysts are provided in Fig. 28. In another work, Bajpai et al. achieved an improved H_2 production rate of 18 mmol h^{-1} g^{-1} with the generation of three VAPs, glycolaldehyde, DHA, and formic acid, from a glycerol–water solution with Au integrated with P25-TiO$_2$ (Au@TiO$_2$).[52] The Au@TiO$_2$ catalyst system achieved 4–10% conversion of 0.05 M glycerol to VAPs. The photocatalytic experiments were carried out under three different reaction conditions (aerobic, anaerobic and dry air) and under 2 different light sources (direct sunlight and one sun condition with 100 mW cm^{-2}). The overall products yield was higher under aerobic conditions and sunlight irradiation compared to anaerobic and dry air conditions. However, 7.5 mmol g^{-1} CO$_2$ was also observed under aerobic conditions due to the over-oxidation of glycerol. The liquid and gaseous products were the same when the photocatalytic experiments were performed under one-sun conditions. However, the CO$_2$ production declined (5.3 mmol g^{-1}) under one sun condition compared to direct sunlight. The dual-function of the catalyst was ascribed to the improved charge transport and efficient separation of photogenerated charge carriers due to the highly dispersed and electronically integrated Au with TiO$_2$. The development of photocatalytic systems that can selectively produce the desired products in high yields from biomass components, without compromising the yield of H_2 is a significant challenge in this area. It should also be noted that a similar concept in the electrolysis of aqueous glycerol has been growing rapidly in the last 3–4 years and a few recent works is worth mentioning. Chauhan et al.[212] achieved a low-voltage pathway to water electrolysis, while producing H_2 at the cathode and value-added products at the anode.

6. Simultaneous oxidation of organic contaminants and hydrogen evolution from wastewater

Industrial and domestic areas produce a huge amount of wastewater daily, which is a serious environmental issue. Furthermore, the treatment of wastewater is an energy consuming process,

Fig. 28 (a) Schematic illustration of the photocatalytic process. Comparison of H_2 production performance of samples with different nickel loadings (b). (c) Glycerol conversion over different photocatalysts. Yield of liquid products obtained with best-performing catalyst (d) and (e) plausible reaction mechanism. Reproduced with permission from ref. 211. Copyright 2023, Elsevier.

whereas wastewater itself is a rich source of energy and it contains four to five times more energy than needed for its treatment. For example, wastewater is a potential source of biohydrogen, a clean energy and a feedstock chemical.[213] The majority of studies on hydrogen generation used pure water as the hydrogen source. Typically, holes oxidise water to make oxygen and photo-generated electrons convert water into hydrogen. However, given that the water oxidation process is a slow process, molecules such as alcohols, organic acids, and triethanolamine are frequently utilised as sacrificial agents to consume the photo-generated holes to increase the hydrogen production efficiency, thus making the overall process uneconomical.[213] Recently, many studies have demonstrated that the construction of TiO_2-based photocatalytic systems is thermodynamically advantageous for both the generation of hydrogen and the oxidation of organic contaminants from wastewater.[213–220] Energy production and environmental cleanup are two advantages of using wastewater as a feedstock for photocatalytic hydrogen production. Wastewater contains a variety of organic contaminants that can act as sacrificial agents, consuming photogenerated holes and lowering the recombination rates to increase the efficiency of hydrogen generation. TiO_2 may oxidise common pollutants including dyes, pharmaceuticals, and industrial effluents, facilitating the breakdown process and the generation of hydrogen.[213–216]

Wu et al. developed a dual-functional photocatalyst system for the treatment of pharmaceutical-contaminated water using Co_3O_4-modified {001}/{101}-TiO_2(TC) nanosheets. The unique aspect of this photocatalytic system is that the p-type semiconductor Co_3O_4 creates a p–n junction with TiO_2 and the {001}/{101} facets of TiO_2 form an inherent surface heterojunction, which enhances the charge carrier separation. The electrons on the surface of the TiO_2 nanosheet can convert water molecules into molecular hydrogen, while the holes on the Co_3O_4 surface effectively oxidise pharmaceutical contaminants in the wastewater.[213] The interesting idea of the concurrent utilization of electrons and holes was employed by Salgaonkar for different isomers of butanol oxidation to the corresponding butanal/butanone and hydrogen with TiO_2–Pd and Pd coated with half-a-monolayer of Pt under visible light.[216] This generic procedure for the selective oxidation of alcohol to aldehyde/ketone with H_2 is worth pursuing for many different substrates. The mineralization of a serious endocrine disruptor, namely endosulphan, was investigated by Devaraji et al. with a solid solution of ZnO–ZnS under direct sunlight.[214] The a-TiO_2 (anatase TiO_2)/b-AC (biomass activated carbon) nanocomposite synthesized through the ultrasonication technique was very effective for sulphide wastewater treatment together with excellent photocatalytic hydrogen production (400 mL h^{-1}).[217] Non-metal-doped TiO_2 (NMx-TiO_2, where x is the weight percentage of non-metal element) nanocomposites displayed a high hydrogen production rate and COD elimination simultaneously when employed for waste water treatment.[215] In this case, using a catalyst loading of 4 g L^{-1} and light intensity of 5.93 mW cm^{-2}, 7 wt% P-loaded TiO_2 (P7/TiO_2) could achieve a hydrogen production rate of 8.34 mmol g^{-1} and 50.6% COD elimination.

The simultaneous oxidation of organic waste and water reduction offer a viable solution to major environmental and energy problems. The goal of ongoing research and development is to remove financial and technological obstacles, enabling the utilization of these technologies in everyday life and their public availability. The development of more sophisticated photocatalysts with increased efficiency has been the focus of recent research. Many organic wastes, such as plastic wastes, agricultural, and industrial pollutants, can be efficiently broken down by photocatalytic reactions. This helps in decreasing the environmental problems caused by waste accumulation. Also, the photocatalytic breakdown of harmful organic compounds into less toxic chemicals may reduce the water and soil pollution.

7. Photoreactor setup

The amount of H_2 produced during a photocatalytic process not only depends on the efficiency of the catalyst system, but also on the photoreactor setup. The photoreactor setup plays an important role in the solar to hydrogen (STH) or solar to chemical (STC) conversion efficiency. An ideal photoreactor should facilitate the maximum absorption of incident photons on the catalyst surface with minimal loss. The photoreactor should be designed in such a way that most of the incident irradiation must fall on the surface of the photocatalyst. The classification of photoreactors is based on their mode of operation, number of phases involved, and the type of membrane used.[221] The commonly used photoreactors include slurry type, fixed bed and membrane photoreactors. Annular reactors are the most popular slurry-type photoreactor.[222] Based on the relative positions of the reactor and the light source, annular photoreactors are further classified into externally illuminated photoreactors and internally illuminated photoreactors. Among the fixed-bed photoreactors, monolith, optical fiber, honeycomb, cylindrical and thin film photoreactors are commonly used. The annular reactor is a tubular reactor with a light source located only at its axis.[222] There are some technical and economic challenges in large-scale hydrogen production using photocatalytic reactors, which can only be profitable in terms of energy if the energy output is greater than the energy input. Hassan et al. fabricated an inner-irradiation quartz annular reactor illuminated with a 300 W Xe lamp with vacuum and recirculation pumps, a gas collector and a water-cooled condenser.[223] This photoreactor setup for photocatalytic water splitting reaction in the presence of 0.1 g of TiO_2–CuO composite nanofiber photocatalyst suspended in 1 M KOH solution resulted an H_2 production rate of 2116 and 2715 μmol g^{-1} in an oxygen and air atmosphere, respectively. In a different study, a photoreactor comprised of a flat cylindrical Plexiglas cell, equipped with an optical window made of Pyrex glass and connected to a closed stainless steel system and filled with a photocatalyst bed prepared from 14 mg of Pt/Cu/TiO_2 photocatalyst with different Cu/TiO_2 ratios in the range of 0.05 to 0.5 wt% and 0.5 wt% Pt on quartz beads was used for photocatalytic water splitting reaction using a 20% v/v methanol-water mixture as the hydrogen source and a xenon arc lamp having a 40.0 mW cm^{-2} power density as the light source.[224] Under these

Fig. 29 (a) Digital photograph and (b) schematic diagram of the flow membrane reactor used for photocatalytic methanol dehydrogenation and reforming. (c) H_2 yield obtained with different Cu wt% on PC50. (d) Amount of H_2 produced with 1% Cu/PC50 at different temperatures. (e) Schematic illustration of photocatalytic process on 1% Cu/PC50 in a flow membrane reactor. Reproduced with permission from ref. 226. Copyright©2022, the Royal Society of Chemistry.

conditions, the $Pt/Cu/TiO_2$ photocatalyst containing 0.1 wt% of Cu produced the highest hydrogen production rate of 27.2 mmol h^{-1} g^{-1}.[224] In another variation, by employing a Photo-CREC Water-II (PCW-II) reactor and 0.25 wt% $Pd–TiO_2$ photocatalyst, Rusinque and coworkers generated an H_2 volume of 113 and 29 cm^3 STP under UV and visible light irradiation, respectively, for 6 h.[225] They used 6 L of water and 0.15 g L^{-1} of photocatalyst during the reaction. PCW-II is a slurry-type batch reactor equipped with a storage tank to house the photocatalyst, water and organic scavenger (ethanol). This tank also possesses two ports for gas and liquid phase sampling. The PCW-II reactor has several advantages such as uniform distribution of catalyst with well-mixed suspension, a high surface to volume reactor ratio, negligible catalyst fouling, comparatively higher UV with no internal/external diffusion transport and visible light transmittance (97%), and higher resistance towards chemicals. Generally, most researchers use batch reactors; however, their low mass transfer and limited light penetration constrain the light absorption and H_2 production efficiency of photocatalysts.[226] The above-mentioned drawbacks of batch reactors can be solved if a flow membrane reactor is employed. In this context, a flow membrane reactor was employed for photocatalytic methanol dehydrogenation and reforming. The flow membrane reactor consisted of three major parts including a reactant vessel, reactor and product collector. A detailed schematic diagram and digital photograph of the flow membrane reactor are shown in Fig. 29a and b, respectively. By employing this membrane reactor and a 300 W xenon

lamp (T: 303 K, P: 1 atm), the optimized catalyst (1% Cu/PC50) fabricated in thin film form on a glass fibre membrane exhibited a hydrogen production rate of 25 487 and 33 702 μmol g^{-1} h^{-1} at 303 and 333 K, respectively.[226] The photocatalytic performance and mechanism of the Cu/PC50 photocatalysts are shown in Fig. 29c–e. The H_2 production rate observed with the flow membrane reactor was 1.63-times higher than that obtained with the conventional batch reactor. The enhanced H_2 production efficiency of 1% Cu/PC50 in the flow membrane reactor can be attributed to the improved mass transfer, which subsequently enhanced the adsorption and desorption of the reactants and products during photocatalysis. The implementation of membrane reactors compared to other conventional-type reactors for photocatalytic hydrogen production is not only a cost-effective approach but also enhances the separation, sustainability, yield, and selectivity for H_2.

Conclusion and perspectives

Solar hydrogen production with water as the main hydrogen source employing TiO_2-based semiconductor photocatalysts is a renewable process and an alternative to the steadily increasing demand for energy and the environmental issues pertaining to the increasing consumption of fossil fuels. In this regard, the present review aimed to summarize the research carried out in the last decade in the area of photocatalytic hydrogen evolution. In this review, we highlighted the recent progress in the material

integration aspects by describing the integration of TiO_2 with different categories of materials and how this helps in tailoring the electronic and optical properties for activity tuning in solar H_2 production with water as the main source. The structure–activity correlation of TiO_2-based photocatalysts was emphasized to understand the mechanistic aspects and how the entire photocatalytic hydrogen production area has been progressing. We also discussed the importance of fabricating photocatalysts in thin-film form for enhanced photocatalytic activity and scalability using existing photocatalysts.

The integration of TiO_2-based photocatalysts with a second light-absorbing component and/or co-catalyst can significantly influence their H_2 production rate. Metal nanoparticles in the form of single atoms and clusters reduce the metal loading and improve the catalytic efficiency. The porosity of a photocatalyst influences the solar hydrogen production rate by providing a large number of surface exposed sites and enhances its light-harvesting ability by transferring the incident photon flux into the internal surface of mesoporous TiO_2 through multiple internal reflections and increasing the mass transfer rate. The photocatalysts fabricated in thin-film form show a significantly high performance for solar hydrogen production compared to the same catalysts in particulate form because the catalyst nanoparticles fabricated in thin film are highly connected across the substrate and have a larger exposed surface area to the reactants and sunlight with relatively less mass transfer constraints. The efficient and concurrent utilization of both photogenerated holes and electrons is very important to improve the photocatalytic efficiency of materials and the overall energy efficiency of the process. We also discussed the importance of performing the TiO_2-based photocatalytic water splitting reaction in different reactor setups for enhancing the photocatalytic performance of the material and its scalability.

Continuous and dedicated efforts are needed in the area of photocatalytic hydrogen generation to fabricate commercially viable catalysts in scalable form that are efficient to produce sufficient quanta of charge carriers and their utilization. Thus far, less emphasis has been placed on the scalability and long-term stability of the photocatalytic material. In fact, for real world applications, photocatalysts that can deliver the same performance for several months (or even a year) and their scalability are necessary, and hence focus should be placed on developing novel photocatalysts with exceptional stability together with scalability towards commercial applications. Despite the significant advancements in this field, the solar-to-hydrogen (STH) conversion efficiency still needs to be improved for practical applications. At least 10% STH should be achieved, which is expected to attract industrial attention. Overall water splitting leading to the direct conversion of water into hydrogen without using any sacrificial reagent and by reducing greenhouse gas emission is a promising technique.[227,228] Renewable H_2 production coupled with wastewater treatment with a suitable photocatalyst is another way to compensate for the energy loss at the expense of waste minimization. Renewable H_2 production and the concurrent formation of value-added products by employing a waste biomass component, such as glycerol,[52,212] are an attractive way to minimize waste with concurrent value addition. The oxidation of biomass components occurs at a significantly lower potential than oxygen formation; in addition, electrons and holes are simultaneously used ensure the catalyst stability for a longer period. Hence, continuous research in the above-mentioned directions is needed to improve the energy efficiency of the process by optimising the photocatalyst and reaction conditions.

Conflicts of interest

The authors declare no conflict of interest.

Acknowledgements

References

1 N. S. Lewis and D. G. Nocera, *Proc. Natl. Acad. Sci. U. S. A.*, 2006, **103**, 15729–15736.

2 A. Kalair, N. Abas, M. S. Saleem, A. R. Kalair and N. Khan, *Energy Storage*, 2021, **3**, e135.

3 B. Tudu, N. Nalajala, P. Saikia and C. S. Gopinath, *Sol. RRL*, 2020, **4**, 1900557.

4 (*a*) X. Zong, H. Yan, G. Wu, G. Ma, F. Wen, L. Wang and C. Li, *J. Am. Chem. Soc.*, 2008, **130**, 7176–7177; (*b*) W. Sibo, B. Y. Guan, X. Wang and X. W. David Lou, *J. Am. Chem. Soc.*, 2018, **140**, 15145–15148; (*c*) S. Wang, Y. Wang, S. L. Zhang, S. Q. Zang and X. W. Lou, *Adv. Mater.*, 2019, **31**, 1903404; (*d*) Z. Xiong, Y. Hou, R. Yuan, Z. Ding, W. J. Ong and S. Wang, *Acta Phys.-Chim. Sin.*, 2022, **38**, 2111021.

5 (*a*) Z. Xie, W. Wang, X. Ke, X. Cai, X. Chen, S. Wang, W. Lin and X. Wang, *Appl. Catal., B*, 2023, **325**, 122312; (*b*) Y. Zhang, Z. Yang, D. Zheng, S. Wang, Y. Hou, M. Anpo and G. Zhang, *Int. J. Hydrogen Energy*, 2024, **69**, 372–380; (*c*) M. Chang, Z. Pan, D. Zheng, S. Wang, G. Zhang, M. Anpo and X. Wang, *ChemSusChem*, 2023, **16**, e202202255.

6 (*a*) R. Guan, H. Zhai, J. Li, Y. Qi, M. Li, M. Song, Z. Zhao, J. Zhang, D. Wang and H. Tan, *Appl. Surf. Sci.*, 2020, **507**, 144772; (*b*) Z. Xi, C. Li, L. Zhang, M. Xing and J. Zhang, *Int. J. Hydrogen Energy*, 2014, **39**, 6345–6353.

7 (*a*) M. Wang, J. Ioccozia, L. Sun and Z. Lin, *Energy Environ. Sci.*, 2014, **7**, 2182–2202; (*b*) M. Satish, B. Viswanathan, R. P. Viswanath and C. S. Gopinath, *Chem. Mater.*, 2005, **17**, 6349–6353.

8 H. Tang, M. Xiong, D. Qu, D. Liu, Z. Zhang, Z. Xie, X. Wei, W. Tu and D. Qu, *Nano Energy*, 2015, **15**, 75–82.

9 W. Y. Cheng, T. H. Yu, K. J. Chao and S. Y. Lu, *ChemCatChem*, 2014, **6**, 293–300.

10 L. L. Tan, W. J. Ong, S. P. Chai and A. R. Mohamed, *Appl. Catal., B*, 2015, **166–167**, 251–259.

11 J. Luo, X. Xia, Y. Luo, C. Guan, J. Liu, X. Qi, C. F. Ng, T. Yu, H. Zhang and H. J. Fan, *Adv. Energy Mater.*, 2013, **3**, 737–743.

12 M. Kulkarni, A. Mazare, P. Schmuki and A. Iglic, *Adv. Mater. Lett.*, 2016, **7**, 23–28.

13 M. Luna, M. J. Mosquera, H. Vidal and J. M. Gatica, *Build. Environ.*, 2019, **164**, 106347.

14 W. H. Hung, T. M. Chien and C. M. Tseng, *J. Phys. Chem. C*, 2014, **118**, 12676–12681.

15 S. Liu and H. Syu, *Int. J. Hydrogen Energy*, 2013, **38**, 13856–13865.

16 Y. Wei, J. Xiong, W. Li, R. H. Kollarigowda and G. Cheng, *Inorg. Chem. Front.*, 2018, **5**, 2709–2717.

17 Y. Chen, Z. Mou, S. Yin, H. Huang, P. Yang, X. Wang and Y. Du, *Mater. Lett.*, 2013, **107**, 31–34.

18 K. K. Patra and C. S. Gopinath, *ChemCatChem*, 2016, **8**, 3294–3311.

19 P. K. Sharma, M. A. L. R. M. Cortes, J. W. J. Hamilton, Y. Han, J. A. Byrne and M. Nolan, *Catal. Today*, 2019, **321**, 9–17.

20 (*a*) H. Gong, Q. Liu and C. Huang, *Int. J. Hydrogen Energy*, 2019, **44**, 4821–4831; (*b*) P. Devaraji, N. K. Sathu and C. S. Gopinath, *ACS Catal.*, 2014, **4**, 2844–2853.

21 S. Rajaambal, K. Sivaranjani and C. S. Gopinath, *J. Chem. Sci.*, 2015, **127**, 33–47.

22 S. Martha, P. C. Sahoo, K. M. Parida, P. Chandra Sahoo and K. M. Parida, *RSC Adv.*, 2015, **5**, 61535–61553.

23 M. Z. Rahman, M. G. Kibria and C. B. Mullins, *Chem. Soc. Rev.*, 2020, **49**, 1887–1931.

24 J. Corredor, M. J. Rivero, C. M. Rangel, F. Gloaguen and I. Ortiz, *J. Chem. Technol. Biotechnol.*, 2019, **94**, 3049–3063.

25 A. Savateev and M. Antonietti, *ChemCatChem*, 2019, **11**, 6166–6176.

26 S. Patnaik, S. Martha and K. M. Parida, *RSC Adv.*, 2016, **6**, 46929–46951.

27 G. Zhang, Z. A. Lan and X. Wang, *Chem. Sci.*, 2017, **8**, 5261–5274.

28 X. Li, A. F. Masters and T. Maschmeyer, *Chem. Commun.*, 2017, **53**, 7438–7446.

29 P. Kumar, R. Boukherroub and K. Shankar, *J. Mater. Chem. A*, 2018, **6**, 12876–12931.

30 Y. J. Yuan, Z. T. Yu, D. Q. Chen and Z. G. Zou, *Chem. Soc. Rev.*, 2017, **46**, 603–631.

31 M. Gao, L. Zhu, W. L. Ong, J. Wang and G. W. Ho, *Catal. Sci. Technol.*, 2015, **5**, 4703–4726.

32 D. Zhao and C. F. Yang, *Renewable Sustainable Energy Rev.*, 2016, **54**, 1048–1059.

33 B. Gupta, A. A. Melvin, T. Matthews, S. Dash and A. K. Tyagi, *Renewable Sustainable Energy Rev.*, 2016, **58**, 1366–1375.

34 M. Ge, J. Cai, J. Iocozzia, C. Cao, J. Huang, X. Zhang, J. Shen, S. Wang, S. Zhang, K. Q. Zhang, Y. Lai and Z. Lin, *Int. J. Hydrogen Energy*, 2017, **42**, 8418–8449.

35 V. Kumaravel, S. Mathew, J. Bartlett and S. C. Pillai, *Appl. Catal., B*, 2019, **244**, 1021–1064.

36 R. Shwetharani, M. Sakar, C. A. N. Fernando, V. Binas and R. G. Balakrishna, *Catal. Sci. Technol.*, 2019, **9**, 12–46.

37 M. Ge, Q. Li, C. Cao, J. Huang, S. Li, S. Zhang, Z. Chen, K. Zhang, S. S. Al-Deyab and Y. Lai, *Adv. Sci.*, 2017, **4**, 1–31.

38 A. López Ortiz, M. Meléndez Zaragoza, J. Salinas Gutiérrez, M. Marques Da Silva Paula and V. Collins-Martínez, *Int. J. Hydrogen Energy*, 2015, **40**, 17308–17315.

39 F. Wu, X. Hu, J. Fan, E. Liu and T. Sun, *Plasmonics*, 2013, **8**, 501–508.

40 K. Wu, Y. Shang, H. Li, P. Wu, S. Li, H. Ye, F. Jian, J. Zhu, D. Yang, B. Li and X. Wang, *Molecules*, 2023, **28**, 4350.

41 M. Yasuda, T. Matsumoto and T. Yamashita, *Renewable Sustainable Energy Rev.*, 2018, **81**, 1627–1635.

42 C. S. Gopinath and N. Nalajala, *J. Mater. Chem. A*, 2021, **9**, 1353–1371.

43 S. S. Mani, S. Rajendran, N. Nalajala, T. Mathew and C. S. Gopinath, *Energy Technol.*, 2022, **10**, 2100356.

44 S. Y. Toledo Camacho, A. Rey, M. D. Hernández-Alonso, J. Llorca, F. Medina and S. Contreras, *Appl. Surf. Sci.*, 2018, **455**, 570–580.

45 G. Mishra, K. M. Parida and S. K. Singh, *ACS Sustainable Chem. Eng.*, 2015, **3**, 245–253.

46 L. Peng, Y. Liu, Y. Li, F. Teng, A. Tang and Y. Yin, *Nanoscale*, 2019, **11**, 22575–22584.

47 Q. Gu, Z. Gao, S. Yu and C. Xue, *Adv. Mater. Interfaces*, 2016, **3**, 17–21.

48 M. A. Khan, M. Al-Oufi, A. Toseef, M. A. Nadeem and H. Idriss, *Catal. Lett.*, 2018, **148**, 1–10.

49 G. Zhang, Z. Zhao, H. Tan, H. Zhao, D. Qu, M. Zheng, W. Yu and Z. Sun, *RSC Adv.*, 2015, **5**, 21237–21241.

50 C. Chen, L. Kuai, Y. Chen, Q. Wang, E. Kan and B. Geng, *RSC Adv.*, 2015, **5**, 98254–98259.

51 R. Camposeco, S. Castillo, V. Rodriguez-Gonzalez, M. Hinojosa-Reyes and I. Mejía-Centeno, *J. Photochem. Photobiol., A*, 2018, **356**, 92–101.

52 H. Bajpai, I. Chauhan, K. N. Salgaonkar, N. B. Mhamane and C. S. Gopinath, *RSC Sustainability*, 2023, **1**, 481–493.

53 B. Tudu, N. Nalajala, K. Prabhakar Reddy, P. Saikia and C. S. Gopinath, *ACS Sustainable Chem. Eng.*, 2021, **9**, 13915–13925.

54 R. M. Mohamed, M. W. Kadi and A. A. Ismail, *Ceram. Int.*, 2020, **46**, 15604–15612.

55 M. Ameen Sha, P. Chandrasekharan Meenu, V. Sasidharan Sumi, T. Chithrajakumary Bhagya, B. Revamma Sreelekshmy and S. M. A. Shibli, *Mater. Sci. Semicond. Process.*, 2020, **105**, 104742.

56 S. A. Rawool, M. R. Pai, A. M. Banerjee, A. Arya, R. S. Ningthoujam, R. Tewari, R. Rao, B. Chalke, P. Ayyub, A. K. Tripathi and S. R. Bharadwaj, *Appl. Catal., B*, 2018, **221**, 443–458.

57 G. Sadanandam, K. Lalitha, V. D. Kumari, M. V. Shankar and M. Subrahmanyam, *Int. J. Hydrogen Energy*, 2013, **38**, 9655–9664.

58 D. Pan, Z. Han, Y. Miao, D. Zhang and G. Li, *Appl. Catal., B*, 2018, **229**, 130–138.

59 Q. Chen, R. Tong, X. Chen, Y. Xue, Z. Xie, Q. Kuang and L. Zheng, *Catal. Sci. Technol.*, 2018, **8**, 1296–1303.

60 L. Clarizia, G. Vitiello, R. Bericat Vadell, J. Sá, R. Marotta, I. Di Somma, R. Andreozzi and G. Luciani, *Int. J. Mol. Sci.*, 2023, **24**, 2004.

61 P. A. Bharad, A. V. Nikam, F. Thomas and C. S. Gopinath, *ChemistrySelect*, 2018, **3**, 12022–12030.

62 H. Bajpai, K. K. Patra, R. Ranjan, N. Nalajala, K. P. Reddy and C. S. Gopinath, *ACS Appl. Mater. Interfaces*, 2020, **12**, 30420–30430.

63 A. Gautam, Y. T. Prabhu and U. Pal, *New J. Chem.*, 2021, **45**, 10257–10267.

64 T. R. Kuo, H. J. Liao, Y. T. Chen, C. Y. Wei, C. C. Chang, Y. C. Chen, Y. H. Chang, J. C. Lin, Y. C. Lee, C. Y. Wen, S. S. Li, K. H. Lin and D. Y. Wang, *Green Chem.*, 2018, **20**, 1640–1647.

65 Z. Zhang, C. Shao, X. Li, Y. Sun, M. Zhang, J. Mu, P. Zhang, Z. Guo and Y. Liu, *Nanoscale*, 2013, **5**, 606–618.

66 B. Tudu, N. Nalajala, K. Reddy, P. Saikia and C. S. Gopinath, *ACS Appl. Mater. Interfaces*, 2019, **11**, 32869–32878.

67 M. M. Kumari, A. Priyanka, B. Marenna and P. Haridoss, *RSC Adv.*, 2017, **7**, 7203–7209.

68 M. A. Alcudia-ramos, M. O. Fuentez-torres, F. Ortiz-chi and C. G. Espinosa-gonzález, *Ceram. Int.*, 2020, **46**, 38–45.

69 P. Devaraji and C. S. Gopinath, *Int. J. Hydrogen Energy*, 2018, **43**, 601–613.

70 P. A. Bharad, K. Sivaranjani and C. S. Gopinath, *Nanoscale*, 2015, **7**, 11206–11215.

71 A. A. Melvin, P. A. Bharad, K. Illath, M. P. Lawrence and C. S. Gopinath, *ChemistrySelect*, 2016, **1**, 917–923.

72 Q. Zhang, P. Chen, L. Chen, M. Wu, X. Dai, P. Xing, H. Lin, L. Zhao and Y. He, *J. Colloid Interface Sci.*, 2020, **568**, 117–129.

73 Y. Wang, M. Fiaz, J. Kim, N. Carl and Y. K. Kim, *ACS Appl. Energy Mater.*, 2023, **6**, 5197–5206.

74 X. Yao, X. Hu, Y. Cui, J. Huang, W. Zhang, X. Wang and D. Wang, *Chinese Chem. Lett.*, 2021, **32**, 750–754.

75 L. Zani, M. Melchionna, T. Montini and P. Fornasiero, *J. Phys. Energy*, 2021, **3**, 031001.

76 A. A. Melvin, K. Illath, T. Das, T. Raja, S. Bhattacharyya and C. S. Gopinath, *Nanoscale*, 2015, **7**, 13477–13488.

77 C. Beasley, M. Kumaran Gnanamani, E. Santillan-Jimenez, M. Martinelli, W. D. Shafer, S. D. Hopps, N. Wanninayake and D. Y. Kim, *ChemistrySelect*, 2020, **5**, 1013–1019.

78 M. J. Rivero, O. Iglesias, P. Ribao and I. Ortiz, *Int. J. Hydrogen Energy*, 2019, **44**, 101–109.

79 M. Ismael, *New J. Chem.*, 2019, **43**, 9596–9605.

80 S. Ida, K. Sato, T. Nagata, H. Hagiwara, M. Watanabe, N. Kim, Y. Shiota, M. Koinuma, S. Takenaka, T. Sakai, E. Ertekin and T. Ishihara, *Angew. Chem., Int. Ed.*, 2018, **130**, 9211–9215.

81 Y. Ma, R. Chong, F. Zhang, Q. Xu, S. Shen, H. Han and C. Li, *Phys. Chem. Chem. Phys.*, 2014, **16**, 17734–17742.

82 J. B. Priebe, M. Karnahl, H. Junge, M. Beller, D. Hollmann and A. Brückner, *Angew. Chem., Int. Ed.*, 2013, **52**, 11420–11424.

83 A. L. Luna, E. Novoseltceva, E. Louarn, P. Beaunier, E. Kowalska, B. Ohtani, M. A. Valenzuela, H. Remita and C. Colbeau-Justin, *Appl. Catal., B*, 2016, **191**, 18–28.

84 C. Ban, B. Li, J. Ma, Y. Feng, C. Lin, Y. Chen, Y. Wang, Y. Duan, K. Zhou, L. Gan, S. Wang and X. Zhou, *Ceram. Int.*, 2024, **50**, 15444–15451.

85 C. Zhao, A. Krall, H. Zhao, Q. Zhang and Y. Li, *Int. J. Hydrogen Energy*, 2012, **37**, 9967–9976.

86 R. A. Rather, S. Singh and B. Pal, *Sol. Energy Mater. Sol. Cells*, 2019, **160**, 463–469.

87 X. Hu, L. Xiao, X. Jian and W. Zhou, *J. Wuhan Univ. Technol., Mater. Sci. Ed.*, 2017, **32**, 67–75.

88 M. An, L. Li, Y. Tian, H. Yu and Q. Zhou, *RSC Adv.*, 2018, **8**, 18870–18879.

89 U. Kerketta, H. Kim, N. Denisov and P. Schmuki, *Adv. Energy Mater.*, 2024, **14**, 2302998.

90 M. Shahrezaei, S. M. H. Hejazi, H. Kmentova, V. Sedajova, R. Zboril, A. Naldoni and S. Kment, *ACS Appl. Mater. Interfaces*, 2023, **15**, 37976–37985.

91 I. Mondal, S. Gonuguntla and U. Pal, *J. Phys. Chem. C*, 2019, **123**, 26073–26081.

92 V. Jovic, K. E. Smith, H. Idriss and G. I. N. Waterhouse, *ChemSusChem*, 2015, **8**, 2551–2559.

93 M. Z. Ge, C. Y. Cao, S. H. Li, Y. X. Tang, L. N. Wang, N. Qi, J. Y. Huang, K. Q. Zhang, S. S. Al-Deyab and Y. K. Lai, *Nanoscale*, 2016, **8**, 5226–5234.

94 Y. Choi, H. I. Kim, G. H. Moon, S. Jo and W. Choi, *ACS Catal.*, 2016, **6**, 821–828.

95 J. Nie, A. O. T. Patrocinio, S. Hamid, F. Sieland, J. Sann, S. Xia, D. W. Bahnemann and J. Schneider, *Phys. Chem. Chem. Phys.*, 2018, **20**, 5264–5273.

96 P. Zhuang, H. Yue, H. Dong and X. Zhou, *New J. Chem.*, 2020, **44**, 5428–5437.

97 M. A. Eldoma, S. O. Alaswad, M. A. Mahmoud, I. Y. Qudsieh, M. Hassan, O. Y. Bakather, G. A. Elawadi, A. F. F. Abouatiaa, M. S. Alomar, M. S. Elhassan, I. G. Alhindawy and Z. M. Ahmed, *J. Photochem. Photobiol., A*, 2024, **446**, 115164.

98 L. Clarizia, G. Vitiello, G. Luciani, I. Di Somma, R. Andreozzi and R. Marotta, *Appl. Catal., A*, 2016, **518**, 142–149.

99 N. L. Reddy, S. Kumar, V. Krishnan, M. Sathish and M. V. Shankar, *J. Catal.*, 2017, **350**, 226–239.

100 L. S. Almazroai and R. E. El-Mekawy, *RSC Adv.*, 2019, **9**, 24670–24681.

101 W. T. Chen, A. Chan, D. Sun-Waterhouse, J. Llorca, H. Idriss and G. I. N. Waterhouse, *J. Catal.*, 2018, **367**, 27–42.

102 S. Gullapelli, M. S. Scurrell and D. K. Valluri, *Int. J. Hydrogen Energy*, 2017, **42**, 15031–15043.

103 H. Huang, J. Lin, L. Fan, X. Wang, X. Fu and J. Long, *J. Phys. Chem. C*, 2015, **119**, 10478–10492.

104 P. Zhang, T. Song, T. Wang and H. Zeng, *RSC Adv.*, 2017, 7, 17873–17881.

105 W. T. Chen, A. Chan, D. Sun-Waterhouse, T. Moriga, H. Idriss and G. I. N. Waterhouse, *J. Catal.*, 2015, **326**, 43–53.

106 K. K. Patra, P. A. Bharad, V. Jain and C. S. Gopinath, *J. Mater. Chem. A*, 2019, **7**, 3179–3189.

107 M. Sathish, R. P. Viswanath and C. S. Gopinath, *J. Nanosci. Nanotechnol.*, 2009, **9**, 423–432.

108 K. Liu, C. Su and T. Perng, *RSC Adv.*, 2015, **5**, 88367–88374.

109 M. Sun, Y. Jiang, M. Tian, H. Yan, R. Liu and L. Yang, *RSC Adv.*, 2019, **9**, 11443–11450.

110 S. K. Khore, N. V. Tellabati, S. K. Apte, S. D. Naik, P. Ojha, B. B. Kale and R. S. Sonawane, *RSC Adv.*, 2017, **7**, 33029–33042.

111 X. Zhou, V. Häublein, N. Liu, N. T. Nguyen, E. M. Zolnhofer, H. Tsuchiya, M. S. Killian, K. Meyer, L. Frey and P. Schmuki, *Angew. Chem., Int. Ed.*, 2016, **55**, 3763–3767.

112 D. Gogoi, A. Namdeo and A. Kumar, *Int. J. Hydrogen Energy*, 2020, **45**, 2729–2744.

113 S. Rajaambal, M. Mapa and C. S. Gopinath, *Dalton Trans.*, 2014, **43**, 12546–12554.

114 (*a*) M. Mapa, K. Sivaranjani, D. S. Bhange, B. Saha, P. Chakraborty, A. K. Viswanath and C. S. Gopinath, *Chem. Mater.*, 2010, **22**, 565–578; (*b*) M. Mapa and C. S. Gopinath, *Chem. Mater.*, 2009, **21**, 351–359.

115 L. K. Preethi, R. P. Antony, T. Mathews, S. C. J. Loo, L. H. Wong, S. Dash and A. K. Tyagi, *Int. J. Hydrogen Energy*, 2016, **41**, 1–13.

116 C. Peng, W. Xu, P. Wei, M. C. Liu, L. Guo, P. Wu, K. Zhang, Y. Cao, H. Wang, H. Yu, F. Peng and X. Yan, *Int. J. Hydrogen Energy*, 2019, **44**, 29975–29985.

117 M. V. Dozzi, G. L. Chiarello, M. Pedroni, S. Livraghi, E. Giamello and E. Selli, *Appl. Catal., B*, 2017, **209**, 417–428.

118 S. S. Lee, H. Bai, Z. Liu and D. D. Sun, *Appl. Catal., B*, 2013, **140–141**, 68–81.

119 G. D. Moon, J. B. Joo, I. Lee and Y. Yin, *Nanoscale*, 2014, **6**, 12002–12008.

120 Y. J. Yuan, G. Fang, D. Chen, Y. Huang, L. X. Yang, D. P. Cao, J. Wang, Z. T. Yu and Z. G. Zou, *Dalton Trans.*, 2018, **47**, 5652–5659.

121 R. Peng, C. Lin, J. Baltrusaitis, C. M. Wu, N. M. Dimitrijevic, T. Rajh, S. May and R. T. Koodali, *Phys. Chem. Chem. Phys.*, 2014, **16**, 2048–2061.

122 S. Shenoy, E. Jang, T. J. Park, C. S. Gopinath and K. Sridharan, *Appl. Surf. Sci.*, 2019, **483**, 696–705.

123 M. T. Uddin, Y. Nicolas, C. Olivier, W. Jaegermann, N. Rockstroh, H. Junge and T. Toupance, *Phys. Chem. Chem. Phys.*, 2017, **19**, 19279–19288.

124 T. N. Ravishankar, M. De Oliveira Vaz, S. Khan, T. Ramakrishnappa, S. R. Teixeira, G. R. Balakrishna, G. Nagaraju and J. Dupont, *New J. Chem.*, 2016, **40**, 3578–3587.

125 W. Wang, S. Zhu, Y. Cao, Y. Tao, X. Li, D. Pan, D. L. Phillips, D. Zhang, M. Chen, G. Li and H. Li, *Adv. Funct. Mater.*, 2019, **29**, 1901958.

126 M. Altomare, N. T. Nguyen, S. Hejazi and P. Schmuki, *Adv. Funct. Mater.*, 2018, **28**, 1704259.

127 M. N. Ha, F. Zhu, Z. Liu, L. Wang, L. Liu, G. Lu and Z. Zhao, *RSC Adv.*, 2016, **6**, 21111–21118.

128 J. D. Lin, S. Yan, Q. D. Huang, M. T. Fan, Y. Z. Yuan, T. T. Y. Tan and D. W. Liao, *Appl. Surf. Sci.*, 2014, **309**, 188–193.

129 H. Zhu, C. Zhen, X. Chen, S. Feng, B. Li, Y. Du, G. Liu and H. M. Cheng, *Sci. Bull.*, 2022, **67**, 2420–2427.

130 X. Wang, H. Dong, Z. Hu, Z. Qi and L. Li, *Mater. Sci. Eng. B*, 2017, **219**, 10–19.

131 C. Wang, X. Cai, Y. Chen, Z. Cheng, X. Luo, S. Mo, L. Jia, R. Shu, P. Lin, Z. Yang, S. Sun, E. Pu and Y. Shen, *Int. J. Hydrogen Energy*, 2017, **42**, 17063–17074.

132 A. Jakimińska, K. Spilarewicz and W. Macyk, *Nanoscale Adv.*, 2023, **5**, 1926–1935.

133 I. Tamiolakis, I. T. Papadas, K. C. Spyridopoulos and G. S. Armatas, *RSC Adv.*, 2016, **6**, 54848–54855.

134 T. N. Ravishankar, M. de, O. Vaz, S. Khan, T. Ramakrishnappa, S. R. Teixeira, G. R. Balakrishna, G. Nagaraju and J. Dupont, *ChemistrySelect*, 2016, **1**, 2199–2206.

135 Y. Liu and C. Tang, *Russ. J. Phys. Chem. A*, 2016, **90**, 1042–1048.

136 W. Chen, S. Yu, Y. Zhong, X. B. Fan, L. Z. Wu and Y. Zhou, *New J. Chem.*, 2018, **42**, 4811–4817.

137 Y. J. Yuan, Z. J. Ye, H. W. Lu, B. Hu, Y. H. Li, D. Q. Chen, J. S. Zhong, Z. T. Yu and Z. G. Zou, *ACS Catal.*, 2016, **6**, 532–541.

138 D. Zhao, Q. Wu, S. Wang, C. Zhao and C. Yang, *Res. Chem. Intermed.*, 2016, **42**, 5479–5493.

139 L. Guo, Z. Yang, K. Marcus, Z. Li, B. Luo, L. Zhou, X. Wang, Y. Du and Y. Yang, *Energy Environ. Sci.*, 2018, **11**, 106–114.

140 X. J. Lv, S. X. Zhou, C. Zhang, H. X. Chang, Y. Chen and W. F. Fu, *J. Mater. Chem.*, 2012, **22**, 18542–18549.

141 D. Xu, L. Li, R. He, L. Qi, L. Zhang and B. Cheng, *Appl. Surf. Sci.*, 2018, **434**, 620–625.

142 H. An, M. Li, W. Wang, Z. Lv, C. Deng, J. Huang and Z. Yin, *Ceram. Int.*, 2019, **45**, 14976–14982.

143 W. Liu, L. Wang, T. Chin, Y. Yen and T. Perng, *RSC Adv.*, 2018, **8**, 30642–30651.

144 J. Wang, J. Huang, H. Xie and A. Qu, *Int. J. Hydrogen Energy*, 2014, **39**, 6354–6363.

145 S. A. Hassanzadeh-Tabrizi, C. C. Nguyen and T. O. Do, *Appl. Surf. Sci.*, 2019, **489**, 741–754.

146 S. Kamalakannan, N. Balasubramaniyan, N. Bernaurdshaw and G. Vattikondala, *Nanoscale Adv.*, 2023, **5**, 5907–5922.

147 Y. Tan, Z. Shu, J. Zhou, T. Li, W. Wang and Z. Zhao, *Appl. Catal., B*, 2018, **230**, 260–268.

148 I. Mondal and U. Pal, *New J. Chem.*, 2015, **39**, 6925–6934.

149 L. Kuang and W. Zhang, *RSC Adv.*, 2016, **6**, 2479.

150 S. Pany and K. M. Parida, *Phys. Chem. Chem. Phys.*, 2015, **17**, 8070–8077.

151 J. Ma, X. Tan, F. Jiang and T. Yu, *Catal. Sci. Technol.*, 2017, **7**, 3275.

152 L. Liu, Z. Liu, A. Liu, X. Gu, C. Ge and F. Gao, *ChemSusChem*, 2014, **7**, 618–626.

153 M. Malizia, S. A. Scott, L. Torrente-Murciano, A. M. Boies, T. A. Aljohani and H. G. Baldovi, *Nanomaterials*, 2023, **13**, 2959.

154 A. Kumari, I. Mondal and U. Pal, *New J. Chem.*, 2015, **39**, 713–720.

155 Y. Sun, X. F. Wang, G. Chen, C. H. Zhan, O. Kitao, H. Tamiaki and S. Ichi Sasaki, *Int. J. Hydrogen Energy*, 2017, **42**, 15731–15738.

156 S. Liu, X. Chen, C. Zhang, X. Liu and S. Xu, *Dyes Pigm.*, 2023, **212**, 111128.

157 C. Marchal, T. Cottineau, M. G. Méndez-Medrano, C. Colbeau-Justin, V. Caps and V. Keller, *Adv. Energy Mater.*, 2018, **8**, 1–12.

158 R. A. Rather, S. Singh and B. Pal, *Appl. Catal., B*, 2017, **213**, 9–17.

159 H. Shen, D. Ni, P. Niu, Y. Zhou, T. Zhai and Y. Ma, *Int. J. Hydrogen Energy*, 2017, **42**, 30559–30568.

160 S. B. Kokane, S. D. Sartale, C. A. Betty and R. Sasikala, *RSC Adv.*, 2014, **4**, 55539–55547.

161 K. Manjunath, V. S. Souza, G. Nagaraju, J. Marcos Leite Santos, J. Dupont and T. Ramakrishnappa, *New J. Chem.*, 2016, **40**, 10172–10180.

162 A. K. R. Police, S. V. P. Vattikuti, K. K. Mandari, M. Chennaiahgari, P. S. Phanikrishna, D. K. Valluri and C. Byon, *Ceram. Int.*, 2018, **44**, 11783–11791.

163 H. Li, B. Sun, F. Yang, Z. Wang, Y. Xu, G. Tian, K. Pan, B. Jiang and W. Zhou, *ChemCatChem*, 2017, **9**, 3752.

164 M. Shang, H. Hou, F. Gao, L. Wang and W. Yang, *RSC Adv.*, 2017, **7**, 30051–30059.

165 N. Nalajala, K. K. Patra, P. A. Bharad and C. S. Gopinath, *RSC Adv.*, 2019, **9**, 6094–6100.

166 S. K. Khore, S. R. Kadam, S. D. Naik, B. B. Kale and R. S. Sonawane, *New J. Chem.*, 2018, **42**, 10958–10968.

167 Y. Zhu, Z. Xu, W. Jiang, W. Yin, S. Zhong, P. Gong, R. Qiao, Z. Li and S. Bai, *RSC Adv.*, 2016, **6**, 56800–56806.

168 X. Yang, L. Wu, L. Du and X. Li, *Catal. Lett.*, 2015, **145**, 1771–1777.

169 H. Li, B. Sun, F. Yang, Z. Wang, Y. Xu, G. Tian, K. Pan, B. Jiang and W. Zhou, *RSC Adv.*, 2019, **9**, 7870–7877.

170 J. Wu, S. Lu, D. Ge, L. Zhang, W. Chen and H. Gu, *RSC Adv.*, 2016, **6**, 67502–67508.

171 P. Gomathisankar, T. Noda, H. Katsumata, T. Suzuki and S. Kaneco, *Front. Chem. Sci. Eng.*, 2014, **8**, 197–202.

172 M. Xiao, L. Zhang, B. Luo, M. Lyu, Z. Wang, H. Huang, S. Wang, A. Du and L. Wang, *Angew. Chem., Int. Ed.*, 2020, **59**, 7230–7234.

173 Y. C. Huang, S. Y. Chang and J. M. Jehng, *J. Phys. Chem. C*, 2017, **121**, 19063–19068.

174 B. Yan, J. Zhou, X. Liang, K. Song and X. Su, *Appl. Surf. Sci.*, 2017, **392**, 889–896.

175 I. Majeed, M. A. Nadeem, A. Badshah, F. K. Kanodarwala, H. Ali, M. A. Khan, J. A. Stride and M. A. Nadeem, *Catal. Sci. Technol.*, 2017, **7**, 677–686.

176 Y. Li, B. Wang, S. Liu, X. Duan and Z. Hu, *Appl. Surf. Sci.*, 2015, **324**, 736–744.

177 M. M. Hasan and N. K. Allam, *RSC Adv.*, 2018, **8**, 37219–37228.

178 G. Li, J. Huang, J. Chen, Z. Deng, Q. Huang, Z. Liu, W. Guo and R. Cao, *ACS Omega*, 2019, **4**, 3392–3397.

179 J. Wang, Z. Wang, P. Qu, Q. Xu, J. Zheng, S. Jia, J. Chen and Z. Zhu, *Int. J. Hydrogen Energy*, 2018, **43**, 7388–7396.

180 H. Zhang, F. Liu, H. Wu, X. Cao, J. Sun and W. Lei, *RSC Adv.*, 2017, **7**, 40327–40333.

181 Y. Yang, X. Li, C. Lu and W. Huang, *Catal. Lett.*, 2019, **149**, 2930–2939.

182 J. Xiao, Y. Luo, Z. Yang, Y. Xiang, X. Zhang and H. Chen, *Catal. Sci. Technol.*, 2018, **8**, 2477–2487.

183 W. Wei, X. Liu, S. Cui and J. Liu, *RSC Adv.*, 2017, **7**, 25650–25656.

184 Y. Li, Z. Hu, S. Liu, X. Duan and B. Wang, *React. Kinet., Mech. Catal.*, 2014, **112**, 559–572.

185 C. M. Wu, R. Peng, N. M. Dimitrijevic, T. Rajh and R. T. Koodali, *Int. J. Hydrogen Energy*, 2014, **39**, 127–136.

186 F. Teng, M. Chen, N. Li, X. Hua, K. Wang and T. Xu, *ChemCatChem*, 2014, **6**, 842–847.

187 M. S. Park and M. Kang, *Mater. Lett.*, 2008, **62**, 183–187.

188 E. Cui and G. Lu, *J. Phys. Chem. C*, 2013, **117**, 26415–26425.

189 K. M. Parida, S. Pany and B. Naik, *Int. J. Hydrogen Energy*, 2013, **38**, 3545–3553.

190 N. Rungjaroentawon, S. Onsuratoom and S. Chavadej, *Int. J. Hydrogen Energy*, 2012, **37**, 11061–11071.

191 X. Sun, H. Liu, J. Dong, J. Wei and Y. Zhang, *Catal. Lett.*, 2010, **135**, 219–225.

192 B. Fu, Z. Wu, S. Cao, K. Guo and L. Piao, *Nanoscale*, 2020, **12**, 4895–4902.

193 Y. Chen, L. Soler, C. Cazorla, J. Oliveras, N. G. Bastús, V. F. Puntes and J. Llorca, *Nat. Commun.*, 2023, **14**, 6165.

194 L. Qi, J. Yu and M. Jaroniec, *Phys. Chem. Chem. Phys.*, 2011, **13**, 8915–8923.

195 V. Jovic, Z. H. N. Al-Azri, W. T. Chen, D. Sun-Waterhouse, H. Idriss and G. I. N. Waterhouse, *Top. Catal.*, 2013, **56**, 1139–1151.

196 K. K. Patra and C. S. Gopinath, *J. Phys. Chem. C*, 2018, **122**, 1206–1214.

197 M. Xi, X. Guo, X. Feng, L. Qin, S. Z. Kang and X. Li, *Catal. Lett.*, 2020, **150**, 1368–1372.

198 K. Sivaranjani, S. Rajaambal, T. Das and K. Roy, *ChemCatChem*, 2014, **6**, 522–530.

199 S. Pany, B. Naik, S. Martha and K. Parida, *ACS Appl. Mater. Interfaces*, 2014, **6**, 839–846.

200 F. Wang, R. J. Wong, J. H. Ho, Y. Jiang and R. Amal, *ACS Appl. Mater. Interfaces*, 2017, **9**, 30575–30582.

201 H. Zhang, C. Lin, T. Han, F. Du, Y. Zhao, X. Li and Y. Sun, *ACS Sustainable Chem. Eng.*, 2016, **4**, 6277–6287.

202 T. A. Kandiel, A. A. Ismail and D. W. Bahnemann, *Phys. Chem. Chem. Phys.*, 2011, **13**, 20155–20161.

203 N. K. Sathu, P. Devaraji and C. S. Gopinath, *J. Nanosci. Nanotechnol.*, 2016, **16**, 9203–9208.

204 K. Sivaranjani, S. Agarkar, S. B. Ogale and C. S. Gopinath, *J. Phys. Chem. C*, 2012, **116**, 2581–2587.

205 Y. X. Chen, V. Gombac, T. Montini, A. Lavacchi, J. Filippi, H. A. Miller, P. Fornasiero and F. Vizza, *Green Chem.*, 2018, **20**, 2299–2307.

206 S. S. Mani, S. Rajendran, P. S. Arun, A. Vijaykumar, T. Mathew and C. S. Gopinath, *Energy Adv.*, 2024, **3**, 829–840.

207 (*a*) N. Nalajala, K. N. Salgaonkar, I. Chauhan, S. P. Mekala and C. S. Gopinath, *ACS Appl. Energy Mater.*, 2021, **4**, 13347–13360; (*b*) I. Chauhan, K. K. Patra, H. Bajpai, K. N. Salgaonkar, N. B. Mhamane and C. S. Gopinath, *Dalton Trans.*, 2023, **52**, 2051–2061.

208 A. Naldoni, M. Altomare, G. Zoppellaro, N. Liu, Š. Kment, R. Zbořil and P. Schmuki, *ACS Catal.*, 2019, **9**, 345–364.

209 S. Rajendran, S. S. Mani, T. R. Nivedhitha, A. K. Asoka, P. S. Arun, T. Mathew and C. S. Gopinath, *ACS Appl. Energy Mater.*, 2024, **7**, 104–116.

210 K. N. Salgaonkar, H. Bajpai, N. B. Mhamane, N. Nalajala, I. Chauhan, K. Thakkar, K. Joshi and C. S. Gopinath, *J. Mater. Chem. A*, 2023, **28**, 15168–15182.

211 M. Eisapour, H. Zhao, J. Zhao, T. Roostaei, Z. Li, A. Omidkar, J. Hu and Z. Chen, *J. Colloid Interface Sci.*, 2023, **647**, 255–263.

212 (*a*) I. Chauhan, H. Bajpai, B. Ray, S. K. Kolekar, S. Datar, K. K. Patra and C. S. Gopinath, *ACS Appl. Mater. Interfaces*, 2024, **16**, 26130–26141; (*b*) I. Chauhan, P. M. Vijay, R. Ranjan, K. K. Patra and C. S. Gopinath, *ACS Mater. Au*, 2024, DOI: 10.1021/acsmaterialsau.4c00024; (*c*) A. Saha, M. Vasuntharadevi, R. Ranjan, I. Chauhan, K. K. Patra, H. Bajpai, A. Saha and C. S. Gopinath, *Sustainable Energy Fuels*, 2024, DOI: 10.1039/D4SE00434E.

213 (*a*) Q. Wang, S. Zhu, S. Zhao, C. Li, R. Wang, D. Cao and G. Liu, *Fuel*, 2022, **322**, 124163; (*b*) Y. Wu, Y. Li, H. Hu, G. Zeng and C. Li, *ACS EST Eng.*, 2021, **1**, 603–611.

214 P. Devaraji, M. Mapa, H. M. Abdul Hakeem, V. Sudhakar, K. Krishnamoorthy and C. S. Gopinath, *ACS Omega*, 2017, **2**, 6768–6781.

215 N. Jandam, K. Serivalsatit, M. Hunsom and K. Pruksathorn, *ACS Omega*, 2021, **6**, 24709–24719.

216 K. N. Salgaonkr, S. R. Kale, N. Nalajala, S. Mansuri and C. S. Gopinath, *Chem. Asia J.*, 2023, **18**, e202201239.

217 (*a*) S. Sekar, V. Preethi, V. S. Srivishnu, S. Saravanan and S. Lee, *Int. J. Hydrogen Energy*, 2022, **47**, 40275–40285; (*b*) M. Anthony Raja, V. Preethi, Y. Pal, N. Nalajala and C. S. Gopinath, *J. Phys: Conf. Series*, 2020, **1495** 012035.

218 A. Rioja-Cabanillas, D. Valdesueiro, P. Fernández-Ibáñez and J. A. Byrne, *J. Phys. Energy*, 2020, **3**, 012006.

219 J. Bharatvaj, V. Preethi and S. Kanmani, *Int. J. Hydrogen Energy*, 2018, **43**, 3935–3945.

220 H. A. Maitlo, B. Anand and K. H. Kim, *Appl. Energy*, 2024, **361**, 122932.

221 S. Tasleem and M. Tahir, *J. Environ. Chem. Eng.*, 2021, **9**, 105351.

222 S. Hu, F. Li, Z. Fan and J. Gui, *J. Power Sources*, 2014, **250**, 30–39.

223 M. M. Hasan and N. K. Allam, *RSC Adv.*, 2018, **8**, 37219–37228.

224 M. V. Dozzi, G. L. Chiarello, M. Pedroni, S. Livraghi, E. Giamello and E. Selli, *Appl. Catal., B*, 2017, **209**, 417.

225 B. Rusinque, S. Escobedo and H. D. Lasa, *Catalysts*, 2021, **11**, 405.

226 H. Jiao, J. Yang, X. Li, C. Wang and J. Tang, *Green Chem.*, 2022, **24**, 8345–8354.

227 W. Qian, G. Zhang, W. Xing, Z. Pan, D. Zheng, S. Wang, Y. Hou and X. Wang, *Angew. Chem., Int. Ed.*, 2023, **135**, 202307930.

228 M. Liu, G. Zhang, X. Liang, Z. Pan, D. Zheng, S. Wang, Z. Yu, Y. Hou and X. Wang, *Angew. Chem., Int. Ed.*, 2023, **135**, 202304694.